A neutron scattering study of the quasi-one-dimensional conductor $(TaSe_4)_2I$

1998 J. Phys.: Condens. Matter 10 5039

(http://iopscience.iop.org/0953-8984/10/23/010)

J. Phys.: Condens. Matter **10** (1998) 5039–5068. Printed in the UK PII: S0953-8984(98)91482-5

A neutron scattering study of the quasi-one-dimensional conductor $(TaSe_4)_2I$

J E Lorenzo†¶, R Currat†, P Monceau‡, B Hennion§, H Berger‖ and F Levy‖

† Institut Laue–Langevin, BP 156, 38042 Grenoble Cédex 9, France
‡ Centre de Recherches sur les Très Basses Températures, associé à l'Université Joseph Fourier, CNRS, BP 166, 38042 Grenoble Cédex 9, France
§ Laboratoire Léon Brillouin, Centre d'Etudes de Saclay, 91191 Gif-sur-Yvette Cédex, France
‖ Institut de Physique Appliquée, Ecole Polytechnique Fédérale de Lausanne, CH-1015 Lausanne, Switzerland

Received 10 February 1998

Abstract. The Peierls phase transition in the quasi-one-dimensional conductor $(TaSe_4)_2I$ is investigated by means of elastic and inelastic neutron scattering. The effective critical exponent β, extracted from the temperature dependence of the integrated intensity from the CDW satellite reflections, is anomalously low, suggesting that the phase transition may be of first order. The intensity distribution among symmetry-related satellite reflections indicates a domain structure with slowly fluctuating domain populations. Correlation lengths associated with the diverging 'central peak' are determined and are found to be nearly isotropic, at variance with results obtained on other quasi-one-dimensional compounds, such as platinum chains (KCP) or blue bronze, $K_{0.3}MoO_3$. Doping with 1.2% Nb has a severe effect on the modulated state. The low-temperature satellites are replaced by a diffuse scattering distribution elongated along $\boldsymbol{c}^*$. The absence of a phonon soft mode and the presence of a diverging central peak at the phase transition is interpreted within the framework of strong electron–phonon coupling. Finally, we propose a Ginzburg–Landau phenomenological model, where the interplay between the electronically coupled optical-like order parameter (Ta-atom tetramerization along the chain axis) and the elastic deformations lies at the origin of the phase transition in $(TaSe_4)_2I$.

1. Introduction

Quasi-one-dimensional conductors [1] are unstable under electronic fluctuations which open up gaps on the conduction electron Fermi surface. The result of the electron–lattice interaction is the formation of a charge-density wave (CDW) coupled to a periodic lattice modulation of wavevector $\boldsymbol{q}_s = 2\boldsymbol{k}_F$, where $\boldsymbol{k}_F$ is the conduction band Fermi wavevector.

The quantum description of the CDW instability involves the condensation of electron–hole pairs with total momentum $\pm 2\boldsymbol{k}_F$. The CDW itself can be viewed as resulting from the interference between the right-going $(+2\boldsymbol{k}_F)$ and left-going $(-2\boldsymbol{k}_F)$ condensates [2]. In a weak electron–phonon coupling description, the electronic gap $2\Delta(T)$ and the mean-field transition temperature T_P^{MF} are related through

$$2\Delta(0) = 3.52 k_B T_P^{MF}.$$

¶ Permanent address: Laboratoire de Cristallographie, CNRS, BP 166, 38042 Grenoble Cédex 9, France; e-mail: lorenzo@polycnrs-gre.fr.

0953-8984/98/235039+30$19.50

Experimentally, the ratio between the low-temperature electronic gap and the actual 3D Peierls transition temperature T_P is often found to be much larger than predicted by the above BCS-type relation. This discrepancy is ascribed to the renormalization of the transition temperature ($T_P < T_P^{MF}$) arising from the weak interchain interactions and the large-amplitude 1D fluctuations above T_P [3].

An alternative strong-coupling description has been proposed by Aubry *et al* [4, 5]. For a large enough electron–phonon interaction strength, the electrons become pairwise localized in real space, in what Aubry and co-workers have defined as a dense bipolaronic state. In this latter picture, T_P corresponds to the ordering temperature of the bipolaron fluid, while the gap energy 2Δ corresponds to the binding energy of a single bipolaron. As T_P is of the order of magnitude of the residual (repulsive) interaction energy between bipolarons, one naturally expects to find $T_P \ll 2\Delta/k_B$.

Hence, the validity of the weak-coupling model rests heavily on the assumption of a large ratio between intrachain and interchain interaction energies. The relevant interactions are elastic as much as electronic, as the Peierls instability involves a combined lattice distortion and electronic charge ordering. The anisotropy of the electrical resistivity in the metallic state only reflects the anisotropy of the electronic mean free path and does not provide a proper estimate for the expected anisotropy of the pre-transitional fluctuations.

Direct information on the q-dependent order parameter susceptibility and correlation lengths above T_P can be deduced from diffuse x-ray scattering data. Such measurements have been performed on a few CDW compounds, such as $NbSe_3$ and $K_{0.3}MoO_3$ (for a review of recent work, see [6]). The case of $K_{0.3}MoO_3$ is probably the best documented. Gap measurements, analysed in the weak-coupling framework, suggest a ratio T_P^{MF}/T_P of the order of 2 to 3, depending upon the source [7, 8]. On the other hand, x-ray measurements [9, 10] between T_P = 180 K and room temperature indicate that the ratio of the in-chain ($\xi_\parallel$) to the largest transverse ($\xi_\perp$) correlation length is only a factor of 4. In fact the shortest transverse correlation length is always found to be larger than the relevant interchain distance, so the 1D-fluctuation regime is not observed in that case. Hence, the relevance of weak-coupling theory in the case of $K_{0.3}MoO_3$ is not firmly established, experimentally.

In other quasi-1D CDW systems the situation is less clear due to uncertainty in the value of the gap or due to the absence of direct correlation-length measurements. In 2D CDW systems such as 2H-$TaSe_2$, with $2\Delta(0)/k_BT_P = 28$, it seems clear that weak-coupling theory is no longer applicable [11].

The present work deals with the compound $(TaSe_4)_2I$, which undergoes a Peierls transition near 260 K and for which low-temperature resistivity data [12, 13] and optical data [14] indicate a gap energy of $2\Delta(0) \approx 3000$ K $= 11.5\ k_BT_P$. X-ray results obtained by Fujishita *et al* [15] on $(TaSe_4)_2I$ and on the related compound $(NbSe_4)_2I$, indicate a low correlation-length anisotropy ratio ($1 < \xi_\parallel/\xi_\perp < 2$). However, the accuracy of the x-ray measurements in [15] suffers from resolution limitations and from contamination by non-critical scattering.

In this paper, we show how inelastic neutron scattering can be used to explore the energy scale of the critical fluctuations and to discriminate against non-critical scattering. Over a large temperature range above T_P, the energy scale of the critical fluctuations is narrow enough (a 'central peak') for the correlation lengths to be measurable by elastic three-axis spectrometry. We present neutron scattering results which confirm the low anisotropy of the critical fluctuations (section 3). We suggest that strong interchain interactions arise in this compound due to the long-wavelength acoustic character of the atomic displacements involved in the Peierls distortion.

Section 4 deals with the low-frequency inelastic response (10 GHz–2 THz). We first present room temperature results on acoustic branches propagating along symmetry directions. These results extend previous ultrasonic measurements [16] and provide an overall picture of the acoustic response of $(TaSe_4)_2I$. Second, we focus on the temperature dependence, above and below T_P, of the transverse acoustic phonon branch connected to the Peierls transition around the satellite wavevector, $\boldsymbol{q}_s$. We observe a very limited softening of the acoustic mode at the satellite position (a Kohn anomaly) contrary to what would be expected in a weak-coupling picture.

In section 5 we discuss the above experimental results within the framework of Aubry's strong electron–phonon coupling [4, 5] model. We note that the Peierls transition in $(TaSe_4)_2I$ appears to be of a more complex nature than in other quasi-1D CDW compounds, such as $K_{0.3}MoO_3$. In particular, the sensitivity of the modulation wavevector components to dilute isoelectronic doping makes it difficult to visualize the phase transition in $(TaSe_4)_2I$ as originating purely from Fermi surface effects. This leads us to propose, in section 6, a phenomenological Landau–Ginzburg free energy, based on an optical-like order parameter (Ta-atom tetramerization) interacting with the acoustic degrees of freedom. The model is then shown to account for the strong transverse acoustic character of the atomic displacements and for the finite values of the in-plane and in-chain CDW wavevector components.

2. Electronic structure of $(TaSe_4)_2I$

$(TaSe_4)_2I$ belongs to the family of transition metal tetraselenides $(MSe_4)_nI$ with M = Ta, Nb and $n = 2, 3, 10/3$. The crystal structure of these compounds consists in an arrangement [17] of strongly bonded $(MSe_4)_\infty$ chains parallel to the tetragonal c-axis, separated by strands of iodine ions (cf. figure 1). In each chain, M atoms and Se_4 rectangles alternate, the latter following a nearly regular screw arrangement along $\boldsymbol{c}$ with an angle of approximately 45° between consecutive rectangles. Within the rectangles the shortest Se–Se distance corresponds to that of a Se_2^{2-} dimer. The crystallographic space group in the undistorted metallic state is $I422$ with lattice parameters $a = 9.531$ Å and $c = 12.824$ Å. The body-centred unit cell contains two adjacent chains with four $(TaSe_4)$ units in each chain.

The Peierls transition temperature, as obtained from diffraction and resistivity data [12, 13], varies between 240 K and 265 K, depending on the sample. The low-temperature electrical response shows non-linear effects characteristic of a CDW ground state [12, 13]. X-ray [15] and electron diffraction [18] experiments reveal the formation of an incommensurate distortion below T_P, with a modulation wavevector $\boldsymbol{q}_s = (\pm\eta, \pm\eta, \pm\delta)$ with $\eta = 0.045$ and $\delta = 0.085$ for $(TaSe_4)_2I$ and $\eta = 0.065$ and $\delta = 0.159$ for the isomorphous compound $(NbSe_4)_2I$ ($T_P = 210$ K) [15].

These two compounds are the only ones in the $(MSe_4)_nI$ family to exhibit a unique metal–metal distance ($d = 3.206$ Å) in the high-temperature phase. Consecutive Ta atoms along a chain occupy two alternating slightly non-equivalent sites [17]. XPS measurements [19] distinguish between the two Ta lattice sites while UPS [20] experiments do not. From ionicity considerations, assuming an I^- state for the iodine ions, the two Ta sites formally correspond to Ta^{4+} and Ta^{5+} valence states, with one conduction electron per formula unit. This picture is confirmed by Hall effect [21] and thermopower measurements [22] and by band-structure calculations [23] which suggest a single quarter-filled d_{z^2} electronic band at the Fermi level. Optical data provide evidence for the strong anisotropy in the conductivity ($\sigma_\parallel/\sigma_\perp \approx 500$) between the directions parallel and perpendicular to the chain axis [24].

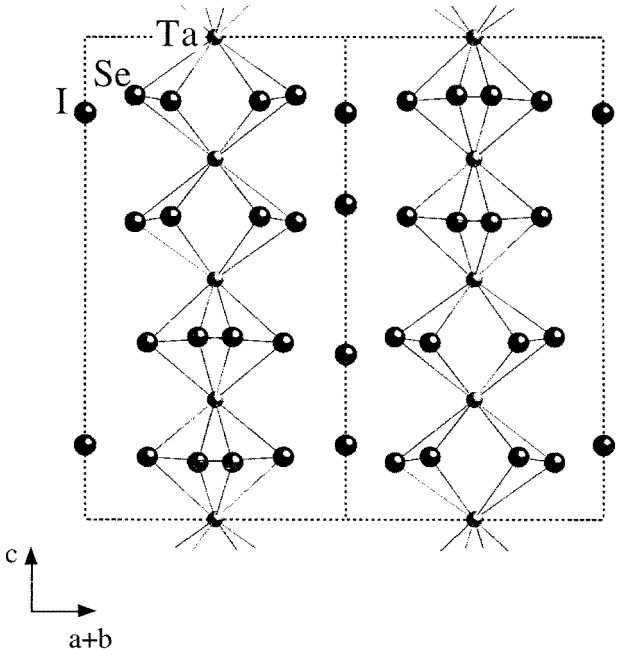

(a)

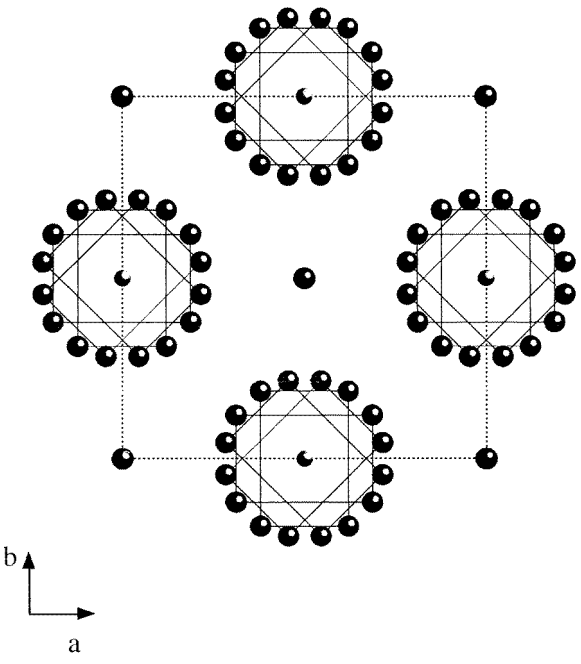

(b)

Figure 1. The structure of $(TaSe_4)_2I$: (a) the projection along [110]; (b) the projection along [001].

The star of the modulation wavevector $\{\boldsymbol{q}_s\}$ spans eight vectors [15, 25]. Performing a detailed analysis of the modulated structure would be difficult because of the large high-temperature unit cell and because of many domain structures possible below T_P. It has not been attempted so far. The satellite extinction rules observed by Fujishita *et al* [15] imply that the atomic displacements are transverse acoustic-like and predominantly polarized in the basal plane (i.e. along $[1\ \bar{1}\ 0]$ for $\boldsymbol{q}_s = (\eta, \eta, \delta)$). A rough fit of selected high-intensity satellites at low temperature [25] shows that the average transverse (in-plane) displacements are four times larger than in the chain direction and are among the largest observed for a CDW system ($\approx$0.087 Å).

Previous inelastic neutron scattering measurements [26, 27] found a spoon-like anomaly on the dispersion curve of the TA branch propagating along $\boldsymbol{q}_s$ and predominantly polarized along $[1\ \bar{1}\ 0]$. Note that, since $\boldsymbol{q}_s$ lies along a general direction in reciprocal space, the mode polarizations and the components of $\boldsymbol{q}_s$ are not fixed by symmetry. However, the fact that the basal-plane components of the modulation wavevector are found to be identical must be connected with a symmetry argument: this is the $2_{x\bar{y}}$ symmetry operation of the space group $I422$ which, independently of time-reversal symmetry, transforms $\boldsymbol{q}_s$ into $-\boldsymbol{q}_s$. Under this condition the group of the wavevector $\boldsymbol{q}_s$ is monoclinic 2. We shall return to this point in section 6.

The small value of the modulation wavevector can be understood on the basis of band-structure arguments. The quarter-filled conduction band leads to a Fermi wavevector $(1/4)(2\pi/d) = c^*$, where $d = c/4$ is the Ta–Ta distance along the chain. Assuming in addition an antiphase arrangement of the CDWs on adjacent chains, one arrives at possible $\boldsymbol{q}_s$-values of $\pm\boldsymbol{a}^* \pm \boldsymbol{c}^*$ or $\pm\boldsymbol{b}^* \pm \boldsymbol{c}^*$, which are equivalent to $\boldsymbol{q}_s = 0$, modulo a body-centred-tetragonal reciprocal-lattice vector. The observed departure of $\boldsymbol{q}_s$ from the Brillouin zone centre may arise from band-structure effects [23] or from a wavevector-dependent coupling between phonon branches. Since it is difficult to understand why electron–phonon interactions should directly affect a long-wavelength transverse acoustic mode. Therefore, Sugai *et al* [28] have developed a phenomenological model in which the phase transition is brought about by the interaction between the acoustic branch and a transverse optical mode coupled to the electronic variables. However, our inelastic neutron scattering measurements [29] have failed to show any evidence for an unstable optical branch below 2 THz.

Correlation lengths are usually obtained from the q-dependence of the frequency-integrated fluctuation spectrum. Our inelastic neutron scattering results on the critical fluctuation spectrum in $(TaSe_4)_2I$ will be presented in section 5 below. We shall see that the TA mode propagating along $\boldsymbol{q}_s$ and polarized along $[1\ \bar{1}\ 0]$ shows a rather limited softening as $T \rightarrow T_P$. Its dispersion *does not* show a local minimum at $\boldsymbol{q} = \boldsymbol{q}_s$, at any temperature. The main temperature-dependent effect is the growth of a central component whose energy width is resolution limited (<10 GHz). The intensity of the central component is found to be at its maximum at $\boldsymbol{q} = \boldsymbol{q}_s$, whereas the frequency-integrated intensity of the TA phonon increases continuously as $\boldsymbol{q} \rightarrow 0$. The sum of the two contributions may or may not go through a maximum at a finite wavevector, depending upon the relative weight of the two contributions. It *will*, in the limit $T \rightarrow T_P$, because the central component dominates. In such a situation it is not clear whether the TA response should be included or not as a part of the critical fluctuation spectrum. In the following, we make the practical choice of using the central component *alone*. This choice affects our results more severely at high temperatures than in the limit $T \rightarrow T_P$. In addition, the fact that the anisotropy of the correlations which we deduce from the present measurements is found to be approximately temperature independent, as expected on theoretical grounds, confirms *a posteriori* the validity of our approach.

3. Elastic scattering experiments: satellite reflections and diffuse scattering

Experiments were carried out on the 4F1, 4F2 and IN12 cold-source three-axis spectrometers installed, respectively, at the Laboratoire Léon Brillouin, Saclay (France) and at the Institut Laue–Langevin, Grenoble (France). For most measurements we used a 5 meV incident-neutron energy ($k_i = 1.55$ Å^{-1} or $\lambda = 4.05$ Å) and tight collimations (25′–25′–20′–20′) in order to optimize the instrumental q-space resolution.

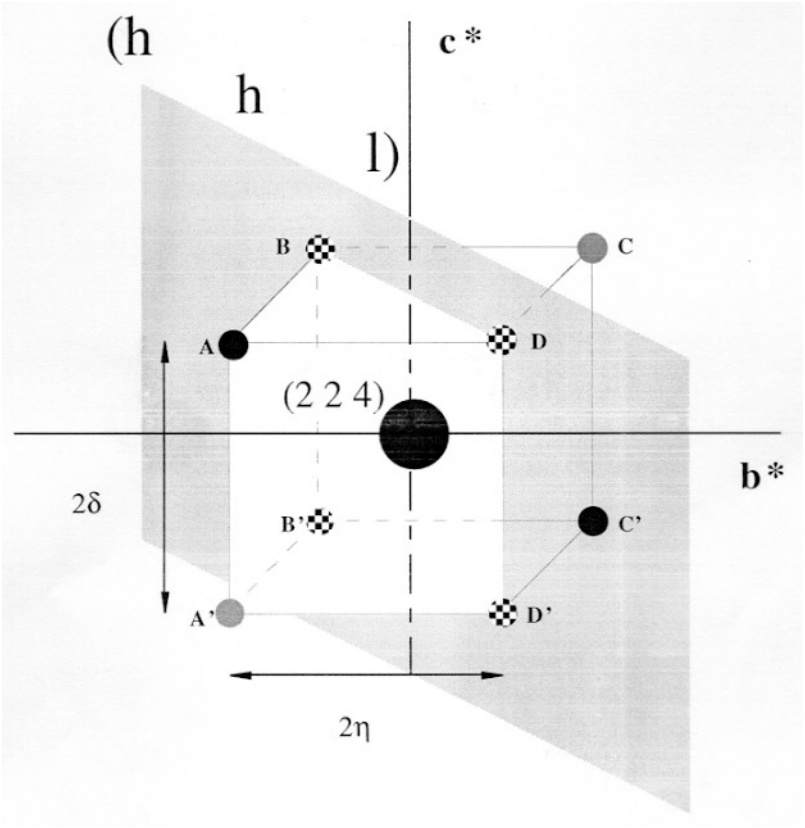

Figure 2. A sketch in reciprocal space of the CDW satellite positions near the (2 2 4) Bragg peak. The shaded plane corresponds to the (h h l) scattering plane. The strong satellites are shown as closed symbols (A, A′, C and C′) and lie outside the scattering plane. They are brought into reflecting positions by tilt adjustments of the sample mount. The chequered symbols (B, B′, D and D′) represent nearly extinct satellites which lie in the scattering plane.

A rod-shaped $4 \times 4 \times 20$ mm^3 specimen, mounted in a closed-cycle refrigerator, was oriented so as to have an (h h l) horizontal scattering zone, as represented by the shaded plane in figure 2. Satellite reflections and diffuse intensities located near the (2 2 4) fundamental Bragg reflection were monitored. Among the eight satellite peaks at $(2 \pm \eta, 2 \pm \eta, 4 \pm \delta)$, the set of four which are located in the (h h l) scattering plane are essentially extinct because the corresponding atomic displacements are along the normal to the scattering plane. The four which are active are indexed as $(2 + \eta, 2 - \eta, 4 \pm \delta)$ and $(2 - \eta, 2 + \eta, 4 \pm \delta)$. They were brought into reflecting positions by means of small goniometer tilt adjustments.

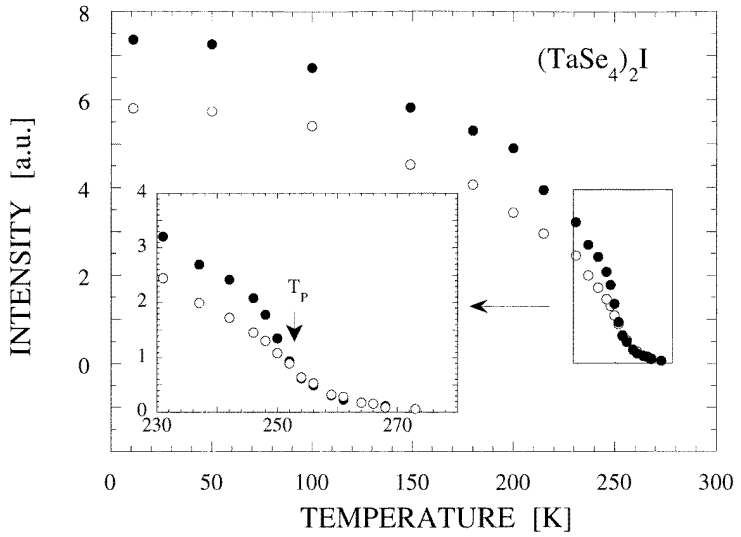

(a)

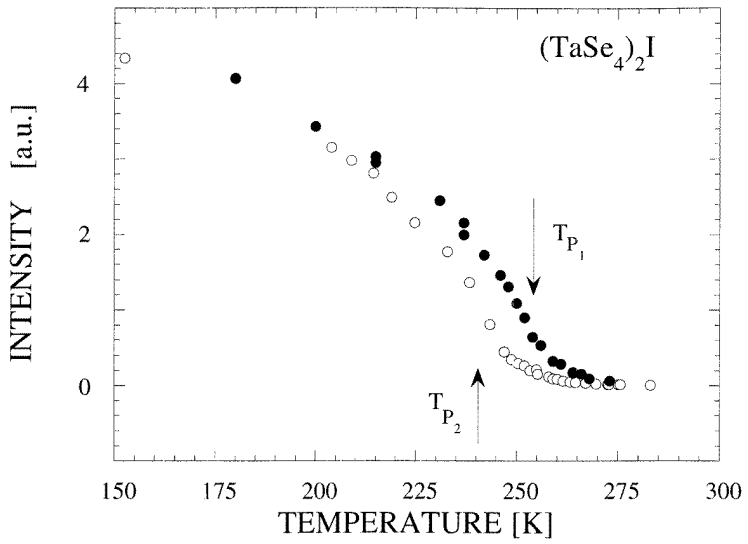

(b)

Figure 3. (a) The temperature variation of the CDW satellite intensity at $(2-\eta, 2+\eta, 4+\delta)$ (full circles) and $(2+\eta, 2-\eta, 4+\delta)$ (open circles). The transition temperature is located at 253 K as shown in the inset. (b) The long-term drift of the transition temperature: the sample in its virgin state (closed circles), $T_{P_1} = 253$ K; the same, two years later, after several cooling and heating cycles (open circles), $T_{P_2} = 241$ K. The intensities are normalized to the value at 150 K.

All three components of the instrumental q-resolution had to be controlled simultaneously. The final trade-off between intensity and resolution yielded the following instrumental q-widths (fwhm): $\Delta q_{\parallel(110)} = 0.008$ Å^{-1}; $\Delta q_{\parallel(001)} = 0.0105$ Å^{-1}; $\Delta q_{\parallel(1\bar{1}0)}$ $(=\Delta q_{\text{vertical}}) = 0.04$ Å^{-1}. The above values have been deduced from scans across the

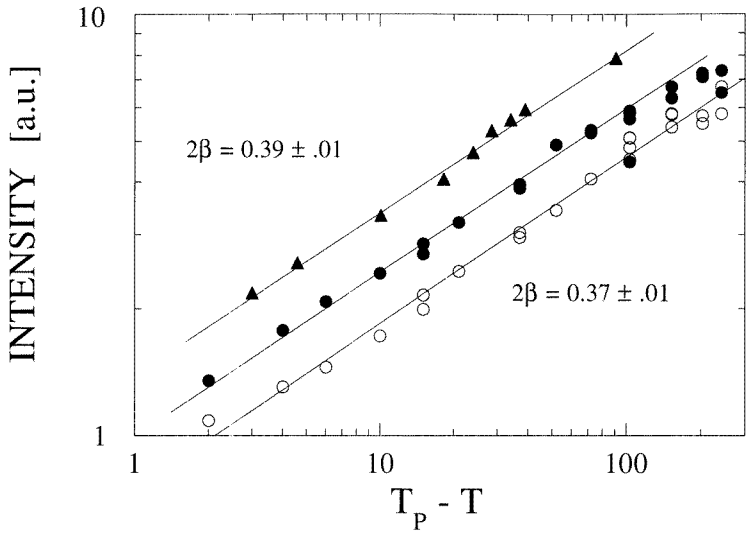

Figure 4. A log–log plot of CDW satellite intensities in $(TaSe_4)_2I$: the circular symbols refer to the same data as in figure 3(a) and the triangles refer to those of figure 3(b). Changes in transition temperature are not correlated with changes in the critical exponent 2β ($I_{sat}(T) \approx (T_P - T)^{2\beta}$).

(2 2 4) reflection and therefore include the effect of sample mosaicity.

In figure 3(a) we present the temperature evolution of the intensity of the satellites located at $\boldsymbol{G}_{224} + \boldsymbol{q}_1 = (2 + \eta, 2 - \eta, 4 + \delta)$ (satellite A in figure 2) and $\boldsymbol{G}_{224} + \boldsymbol{q}_2 = (2 - \eta, 2 + \eta, 4 + \delta)$ (satellite C in figure 2). The transition temperature, as determined from the position of the inflexion point of the curve, is found at $T_P = 253$ K. The intensity tail above T_P is associated with the critical central peak (see section 4).

The scattering vectors for the two satellites in figure 3(a) are related through a symmetry operation of the 422 point group:

$$2_{x,\bar{y}}\{\boldsymbol{G}_{224} + \boldsymbol{q}_1\} = -\{\boldsymbol{G}_{224} + \boldsymbol{q}_2\}.$$

Hence, the intensity ratio of the two satellites gives information on the nature of the modulated state. In particular, the two satellite intensities are expected to be equal if the modulated structure consists in a '4$\boldsymbol{q}$'-state or a '2$\boldsymbol{q}$'-state involving a coherent superposition of $\boldsymbol{q}_1$- and $\boldsymbol{q}_2$-waves. The fact that a systematic intensity difference is observed shows that the modulated structure involves either a 'single-$\boldsymbol{q}$' state, or a '2$\boldsymbol{q}$'-state where $\boldsymbol{q}_1$ and $\boldsymbol{q}_2$ belong to distinct domains. The presence of domains with slowly relaxing populations gives rise to long equilibration times at low temperatures. Below 180 K, after each temperature step, the intensities of the two satellites were found to fluctuate and relax on a timescale much longer than the timescale of the measurements (five minutes per scan).

The two runs shown in figure 3(b) refer to the same specimen as above. They were taken before and after an interval of two years during which the specimen was submitted to several cooling and heating cycles. The transition temperature is seen to be shifted downward by about 10 K in the latter run. The temperature variation of the satellite intensity is however unchanged, as illustrated in figure 4, and so is the satellite position. It has been argued that differences in T_P-values could reflect small deviations from stoichiometry, such as arise from iodine loss. In such a case, one would expect the change in the value of T_P to be correlated with a change in the conduction electron Fermi wavevector, and eventually in

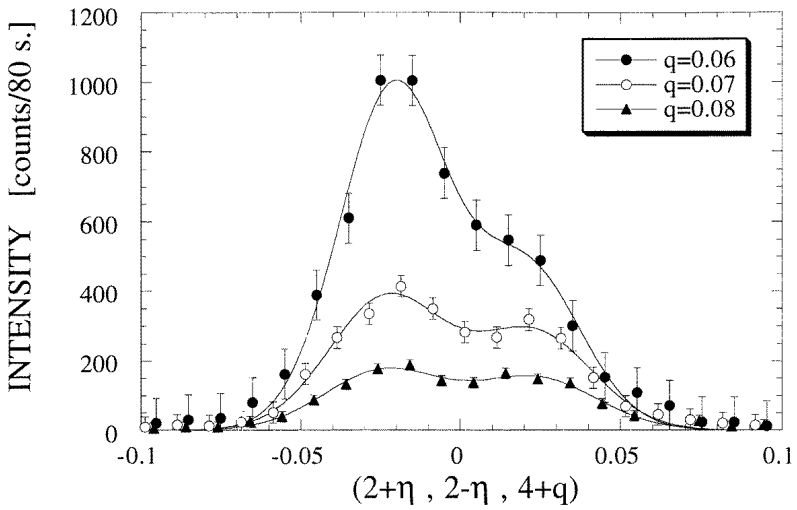

Figure 5. The diffuse scattering profile for $(Ta_{1-x}Nb_xSe_4)_2I$, $x = 1.2\%$.

the satellite position. No such correlation is observed here.

Fitting the integrated satellite intensity to a power law $(T_P - T)^{2\beta}$ yields a value for the critical exponent β of 0.19 ± 0.01, which is even smaller than the classical value at the tricritical point ($\beta = 0.25$), and might indicate that the phase transition is of the first-order type. As was first pointed out by Brezin *et al* [30] and later considered further by Mukamel and Krinsky [31], the anisotropy of the order parameter interactions (i.e. the anisotropy of the fourth- and higher-order terms in the free energy) may affect the critical behaviour for an order parameter with $n \geqslant 4$ components. The presence of a number of components $n \geqslant 4$ makes all fixed points unstable with respect to any anisotropy of the fourth-order free-energy terms and hence one expects the transition to be discontinuous. As in $(TaSe_4)_2I$ the star of the modulation spans eight $\boldsymbol{q}$-positions, such an argument is applicable here, although no jump in the integrated satellite intensity has been detected at T_P. Very recent x-ray measurements of the critical exponents of $(TaSe_4)_2I$ by Requardt *et al* [32] have confirmed the low value of the effective critical exponent β. These authors also suggest that order parameter fluctuations might lie at the origin of the small β-value. We interpret the apparent continuous character of the phase transition as due to blurring by defects and impurities. This view is supported by the large scatter in the observed values of T_P, as shown in figure 3(b).

In what follows we investigate further the effect of impurities by introducing a low concentration of Nb ions substituting for Ta. A batch of Nb-doped samples was prepared by a standard temperature-gradient furnace technique. The nominal Nb concentration was 1.2%. However, chemical analysis performed on several single crystals from the same batch (typical sample size: $5 \times 5 \times 5$ mm^3) showed considerable scatter in the actual bulk Nb content.

The doped sample, studied under similar experimental conditions to those described above, did not produce evidence for low-temperature satellite reflections. Figure 5 shows scans taken at $T = 12.5$ K along $\boldsymbol{a}^* - \boldsymbol{b}^*$, centred around $(2, 2, 4+q)$, for several values of q. The remnants of the two satellite reflections at $(2+\eta, 2-\eta, 4+\delta)$ and $(2-\eta, 2+\eta, 4+\delta)$ now appear as a weak double-peaked intensity distribution centred on $\eta = \pm 0.020$. Along

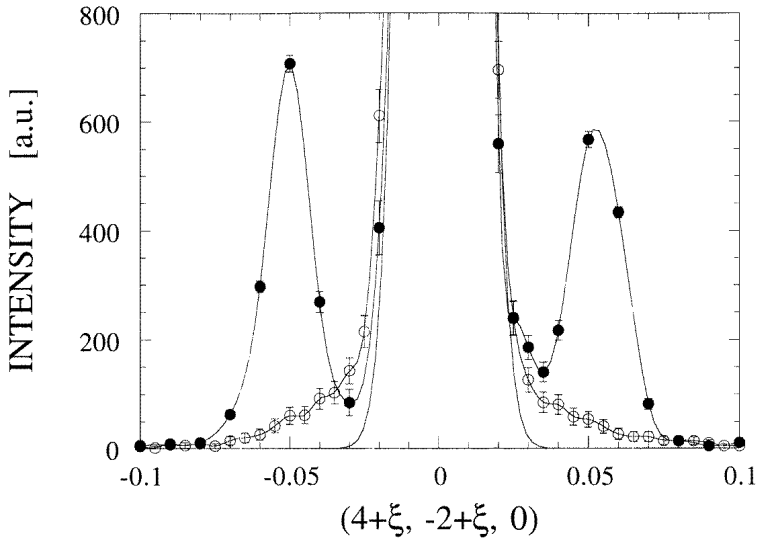

Figure 6. Transverse scans along the $\boldsymbol{a}^* + \boldsymbol{b}^*$ direction in pure $(TaSe_4)_2I$ (closed circles) and in the 1.2%-Nb-doped compound (open circles) at 12.5 K. Both scans have been normalized to the peak intensity of the (4 −2 0) Bragg reflection. The experimental conditions are described in the text.

$\boldsymbol{c}^*$, the diffuse intensity is no longer centred on a finite value of q ($=\delta = 0.085$). Instead, it increases steadily with decreasing q-value. Scans with q-value lower than $0.05c^*$ were not attempted because of possible contamination by the (2 2 4) Bragg reflection.

In figure 6, the intensity distributions for a pure and a Nb-doped sample are compared, using the 4F2 spectrometer operated at an incident-neutron wavevector of $k_i = 1.97$ Å^{-1}, and under somewhat relaxed resolution conditions. The sample was oriented so as to have an (h k 0) horizontal scattering plane and the measurements were performed near the (4 −2 0) Bragg reflection. The q-resolution (fwhm) is 0.02 Å^{-1} in the plane and 0.12 Å^{-1} along the vertical [0 0 1] direction. With this purposely relaxed vertical resolution, the satellites at $(4 + \eta, -2 + \eta, \pm\delta)$, symmetrically located above and below the horizontal scattering plane, are measured simultaneously in a $(4 + \xi, -2 + \xi, 0)$ scan. For the undoped sample (closed circles in figure 6), the three peaks observed correspond to the $(4 - \eta, -2 - \eta, \pm\delta)$ satellites, the (4 −2 0) fundamental peak and the $(4 + \eta, -2 + \eta, \pm\delta)$ satellites (from left to right in the figure; $\eta = 0.05$). The same scan of a doped sample (open circles) only shows wings on both sides of the (4 −2 0) Bragg peak. These wings correspond to diffuse intensity with a finite extension along $\boldsymbol{c}^*$, integrated by the broad vertical resolution of the instrument.

The compounded results shown in figures 5 and 6 suggest that the diffuse intensity in the doped samples is localized around reciprocal-lattice positions of the type ($h \pm 0.02, k \pm 0.02, 0$). The temperature dependence of this intensity, as obtained from figure 6 by integrating across the wings of the distribution, is shown in figure 7 (open symbols). The integrated diffuse intensity shows a much smoother behaviour than the pure-sample satellite intensity (closed symbols). This behaviour appears consistent with resistivity data on similar Nb-doped samples [16], which suggest a diffuse transition at around 200 K.

A detailed and systematic x-ray and neutron scattering study of the incommensurate modulation in the Nb-doped compounds is being currently carried out. Preliminary high-

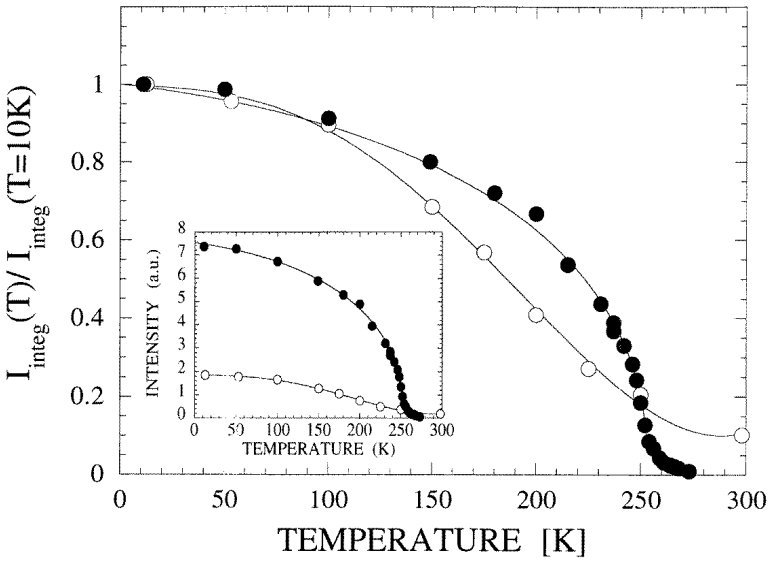

Figure 7. The temperature variation of the CDW satellite intensity in pure $(TaSe_4)_2I$ (closed symbols) compared with the integrated diffuse intensity in the $x = 1.2\%$-Nb-doped compound (open symbols). The data are normalized to their values at low temperatures. The inset shows the satellite intensity normalized to the peak intensity of the (4 −2 0) Bragg reflection.

resolution x-ray data [33] on a 1.2% Nb sample show a well defined modulation wavevector with components $\boldsymbol{q}_s = (0.0322, 0.0322, 0.0388)$, though the peak widths are twice as broad as the instrumental resolution. These results do not contradict those presented above, as the actual amount of Nb in each sample and its degree of homogeneity are not precisely known. The above data confirm the enormous influence of doping on the nature of the low-temperature modulated state. This result is particularly striking in view of the isoelectronic nature of the Nb–Ta substitution.

For pure $(TaSe_4)_2I$ above T_P, we performed elastic ($\omega = 0$) scans through the critical scattering distribution centred at $(2 + \eta, 2 - \eta, 4 + \delta)$ along three orthogonal directions, $\boldsymbol{a}^* + \boldsymbol{b}^*$, $\boldsymbol{a}^* - \boldsymbol{b}^*$ and $\boldsymbol{c}^*$. The scans were corrected for resolution broadening using a standard one-dimensional deconvolution technique. In figures 8(a) and 8(b) we show two typical scans taken at 263 K ($T_P = 241$ K) with the corresponding Lorentzian fits (full line) convoluted with the Gaussian resolution profile (broken line).

The results for the inverse correlation lengths obtained along the three directions $\boldsymbol{c}^*$, $\boldsymbol{a}^* + \boldsymbol{b}^*$, $\boldsymbol{a}^* - \boldsymbol{b}^*$ are plotted in figure 9 as a function of temperature. The different ξ^{-1}-values vary as $([T - T_P]/T_P)^{\nu}$ with $\nu = 0.5$. The anisotropy parameter, given by the ratio $\xi_{c^*}/\xi_{a^*\pm b^*}$, is very small: 1.8 ± 0.2. It is consistent with the anisotropy ratio of 1.5 measured by Fujishita *et al* [34], for the isomorphous compound $(NbSe_4)_2I$, by means of x-ray scattering, but is at variance with that typically found for other quasi-one-dimensional conductors: for $NbSe_3$ and $K_{0.3}MoO_3$, which have two different transverse correlation lengths, the anisotropy ratios amount to 7 and 13, and 4 and 7.5, respectively [34]. From our data shown in figure 9, we find that at 40 K above T_P the transverse correlation length is of the order of 100 Å. The average number of correlated chains can be estimated at $(100/(a/\sqrt{2}))^2 \sim 200$. This clearly reflects the broad temperature extension above T_P of the 3D-fluctuation regime.

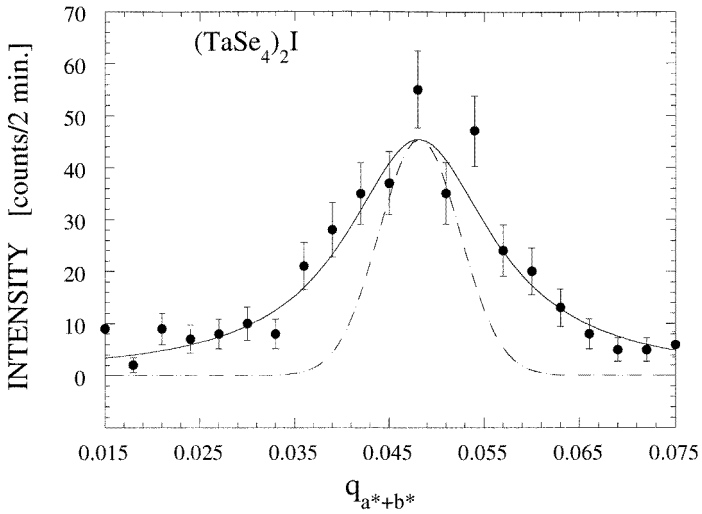

(a)

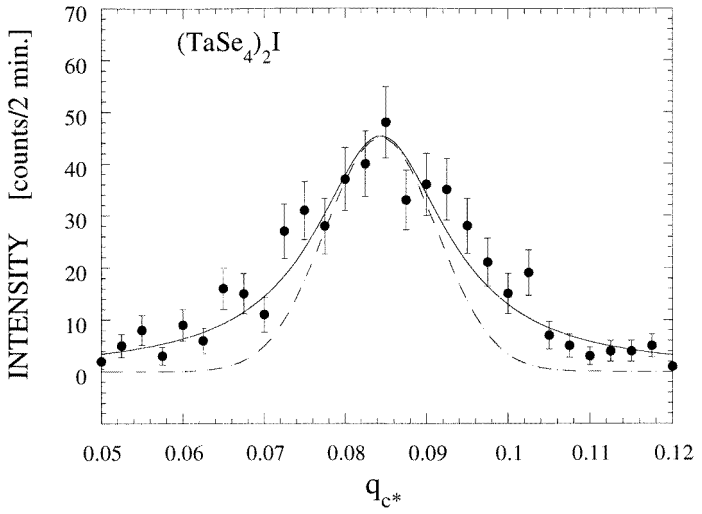

(b)

Figure 8. (a) A scan through the critical scattering distribution, along the $\boldsymbol{a}^* + \boldsymbol{b}^*$ direction. The full line represents the result of a Lorentzian $1/[1+(q\xi)^2]$ fit and the broken line represents the Gaussian instrumental resolution profile along the $\boldsymbol{a}^* + \boldsymbol{b}^*$ direction. (b) As (a), but along the $\boldsymbol{c}^*$-direction ($T = 263$ K; $T_P = 241$ K).

4. Inelastic neutron scattering experiments

Low-frequency measurements ($\omega < 0.5$ THz) were performed on the cold-neutron three-axis spectrometers 4F1 and 4F2 at LLB, and IN12 and IN14 at ILL. A number of incoming-neutron wavevector values were used ($k_i = 1.1$, 1.4, 1.55, 1.64 and 2.0 Å^{-1}) according to the energy-and momentum-transfer requirements. Higher-order neutrons were removed using a beryllium filter ($k_i = 1.1$, 1.4, 1.55 Å^{-1}) or a graphite filter ($k_i = 1.64$ Å^{-1}) or by

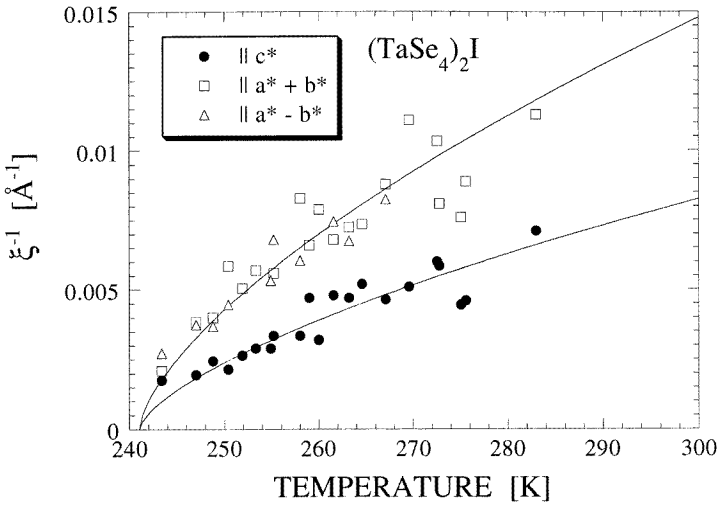

Figure 9. The temperature variation of the Lorentzian halfwidths (the inverses of the correlation lengths) of the critical scattering around $(2+\eta, 2-\eta, 4+\delta)$ along the three directions $\boldsymbol{c}^*$, $\boldsymbol{a}^* + \boldsymbol{b}^*$, $\boldsymbol{a}^* - \boldsymbol{b}^*$ ($T_P = 241$ K). The full lines represent power-law fits, $[(T - T_P)/T_P]^\nu$, with $\nu = 0.5$.

the natural cut-off of the curved neutron guide ($k_i = 2$ Å^{-1} on IN12). The thermal beam three-axis spectrometers IN3 and IN8 at ILL were used for inelastic experiments at energy transfers above $\omega > 0.5$ THz (k_i or $k_F = 2.662$ Å^{-1}).

All of the results presented below correspond to measurements on a nominally pure sample of $(TaSe_4)_2I$, the same sample as the elastic measurements were made on. Preliminary results on the Nb-doped compounds do not show any significant differences, within the limits of experimental accuracy.

4.1. Acoustic branches

In figure 10 we present the room temperature phonon dispersion curves measured along high-symmetry directions. The extrapolated sound velocities are in fair agreement with ultrasonic data [16, 35]. In what follows we summarize the characteristic features of the acoustic dispersions in $(TaSe_4)_2I$.

(i) The transverse acoustic branch propagating along the $\boldsymbol{c}^*$-direction, whose sound velocity is given by $v_{44} = (C_{44}/\rho)^{1/2}$, follows a dispersion law of the type

$$\omega^2(q) = v_{44}^2 q^2 + C^2 q^4 \tag{1}$$

with C denoting a chain-bending force constant ($v_{44} = 450$ m s$^{-1} = 0.71$ THz Å and $C = 5.24$ THz Å^2). The same kind of behaviour is found for the related compound $(NbSe_4)_3I$ at room temperature [36] ($v_{44} = 140$ m s$^{-1} = 0.22$ THz Å and $C = 8.19$ THz Å^2). A similar type of dispersion law is also found for polymer crystals [37] and for layered systems, such as graphite [38], reflecting the one- or two-dimensional bonding anisotropy inherent to these structures. The quasi-one-dimensional character of the $(MSe_4)_nI$ structure is apparent in the elastic properties of all of the compounds of the family, at least at high temperature. It is related to the rigidity of the $(MSe_4)_\infty$ backbone which in turn arises from the directionality of the covalent M–Se bonds.

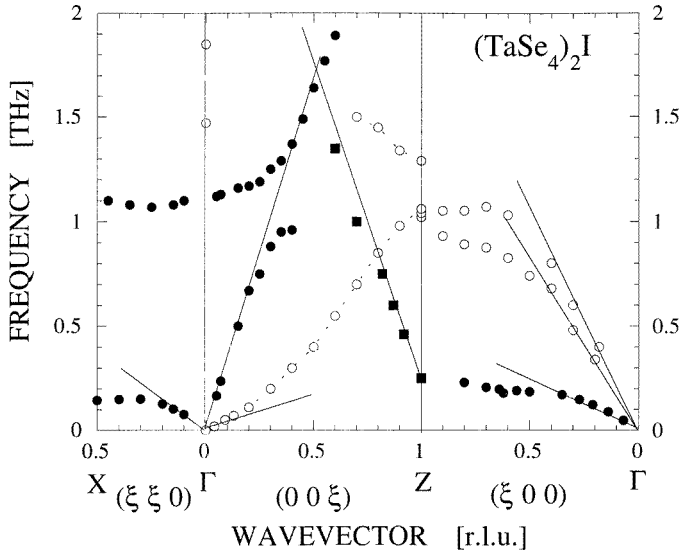

Figure 10. Phonon dispersion curves along high-symmetry directions in $(TaSe_4)_2I$ at room temperature. Modes polarized along the chains (normal to the chains) are shown as closed (open) circles. The sound velocities (solid lines) are taken from the ultrasonic data given in reference [35].

(ii) The z-polarized transverse acoustic modes (TA_z), propagating in the basal plane $[\boldsymbol{a}^*, \boldsymbol{b}^*]$, have the same sound velocity v_{44}. In figure 11 we have plotted the measured acoustic modes that have v_{44} as the sound velocity. The peculiarity of these modes is that they are dispersionless over a large portion of the Brillouin zone, with an extremely low frequency at the zone edge: ≈0.20 THz (see figures 10 and 11). The low-frequency plateau indicates that the $(MSe_4)_\infty$ columns are relatively free to move along the c-direction, independently of each other, due to the weak Se–I–Se interchain bonds.

The TA_z frequency is soft for all wavevectors (q_x, q_y, q_z) in the plane $q_z = 0$. Its dispersion as a function of q_z, for a fixed value of (q_x, q_y), is quite steep as illustrated in figure 10, for the zone boundary Z point. We find

$$\omega^2(q_x, q_y, q_z) \approx \omega^2(q_x, q_y, 0) + v_\parallel^2 q_z^2 \tag{2}$$

where $v_\parallel$ is very close to the longitudinal sound velocity v_{33} along the chain direction. We have argued [39] that the flat and low-frequency TA_z dispersion sheet lies at the origin of the anomalous behaviour of the specific heat [40] and thermal conductivity [41] below 5 K. Such a flat branch is also present in $(NbSe_4)_3I$ at room temperature but it disappears progressively as v_{44} increases below the 273 K ferrodistortive transition [36]. In figure 11 we also show the TA_z dispersion in the $\boldsymbol{a}^*$ and $\boldsymbol{a}^* + \boldsymbol{b}^*$ propagation directions for $(Ta_{1-x}Nb_xSe_4)_2I$ with $x = 1.2\%$ (open symbols). There is no detectable difference between the transverse acoustic mode dispersions for pure and doped crystals.

(iii) The topology of the optical branches is discussed in more detail in reference [29]. In figure 10, we see that the longitudinal acoustic branch along $\boldsymbol{c}^*$ anticrosses a flat mode in the region of 1.1 THz and $\boldsymbol{q}_z = 0.25$–$0.45\ \boldsymbol{c}^*$. By exploiting the symmetry compatibility relations along this direction we conclude that the flat mode has a zone-centre symmetry of A_1 type (totally symmetric, and thus Raman active) or A_2 type (odd with respect to both sets of twofold axes normal to the chain axis, and infrared active in z-polarization). The

peculiarity of this mode is that it is only clearly visible in the region where it anticrosses the LA mode. In the $\boldsymbol{a}^* + \boldsymbol{b}^*$ direction it is hardly visible and its frequency remains constant within experimental accuracy (±0.1 THz). Measurements made below T_P show no detectable change in mode frequencies with temperature. In this frequency range, there are no Raman-active modes [42] whereas far-infrared experiments detect a strong resonance at 1.1 THz (36 cm^{-1}) [43, 44]. A similar resonance has been detected in the blue bronze $K_{0.3}MoO_3$ at 40 cm^{-1} (1.2 THz) [45] and interpreted as a bound collective mode arising from the presence of polarizable impurities. This interpretation has however been questioned by Creager *et al* [46].

4.2. The low-energy acoustic mode around $\boldsymbol{q} = \boldsymbol{q}_s$

As discussed in sections 2 and 3, the satellite structure factor follows closely that of an acoustic mode of wavevector $\boldsymbol{q}_s = (\pm\eta, \pm\eta, \pm\delta) = (\pm 0.045, \pm 0.045, \pm 0.085)$. The atomic displacements involved in the modulation are predominantly transverse to the chain direction and to $\boldsymbol{q}_s$. In figure 2 we illustrate the situation near an $(h\ h\ l)$-type Bragg reflection. The four satellites lying in the scattering plane (shaded plane) are nearly extinct (B, B′, D and D′), while the two pairs located above (A, A′) and below (C, C′) are intense.

The L point of coordinates (0, 0, 0.085), is located midway between the four satellites (A, B, C, D). Along Γ–L the two TA branches are degenerate. Away from the Γ–L direction, the two TA branches split. Figure 12 shows the measured dispersion curves along L → D (lhs) and along L → A (rhs). In each case, only the [1 1 0]-polarized branch is visible. In the direction of the extinct satellite the phonon branch goes up in frequency rapidly. The soft polarization for this satellite wavevector is along [1 $\bar{1}$ 0] and is not visible in the experiment. In the direction of the strong satellite the phonon branch is softer and almost flat between L and A.

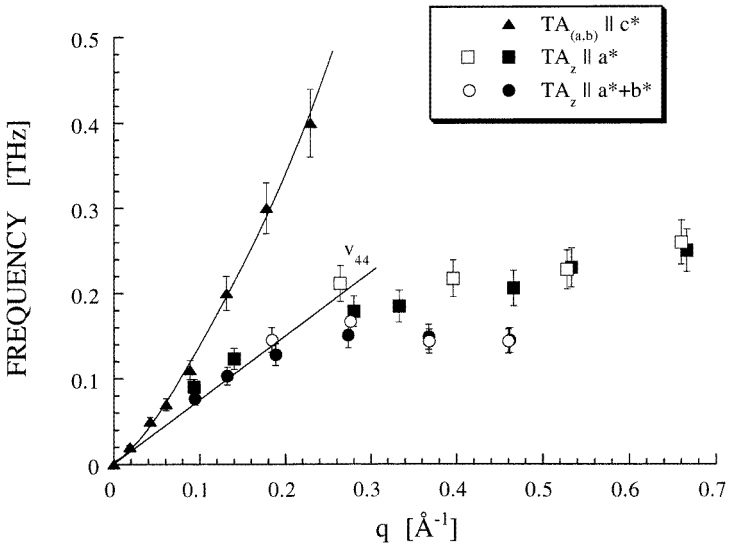

Figure 11. Phonon dispersion curves for the acoustic branches having v_{44} as their sound velocity (room temperature). Closed (open) symbols correspond to pure $(TaSe_4)_2I$ ($(Ta_{1-x}Nb_xSe_4)_2I$, $x = 1.2\%$).

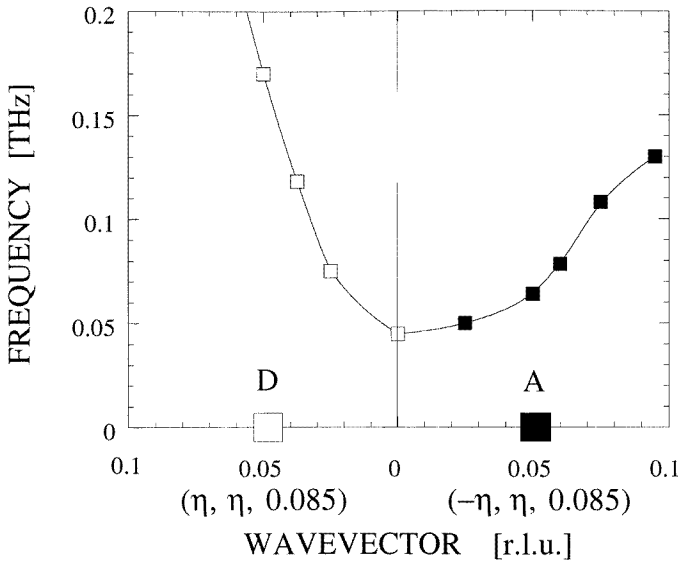

Figure 12. TA phonon dispersion curves for pure $(TaSe_4)_2I$ along the lines D → L (left-hand side) and L → A (right-hand side); room temperature (see figure 2 for the positions of points L, D, A).

The difference between the two TA branches shown in figure 12 illustrates the anomalous character of the mode observed near the strong satellite. Note however that no dispersion minimum is observed at the satellite position, contrary to what would be expected in a standard soft-mode picture. This is consistent with the dispersion measurements along Γ → A, reported by Fujishita *et al* [26], which reveal a spoon-like anomaly but no dispersion minimum at the satellite position. This effect may be viewed as a weak Kohn anomaly or as resulting from the interaction of the TA mode with an optical-mode Kohn anomaly [28].

In figures 13(a) and 13(b) we display the temperature dependence of the soft TA branch at the L point and at the strong-satellite position, respectively. At the L point, the doubly degenerate TA mode at 45 ± 10 GHz shows no measurable temperature variation between 300 K and $T_P = 253$ K. Below T_P, the spectra in figure 13(a) show a growing elastic contamination, which arises from the A and C satellites broadened by finite vertical Q-resolution (cf. figure 2). Otherwise, the inelastic line-shape is unchanged. The energy-integrated inelastic intensity varies as T, as expected from the thermal population factor, and the vertical scales for the scans in figures 13(a) and 13(b) have been normalized accordingly.

A somewhat different behaviour is observed in figure 13(b), for constant-Q scans at satellite position A. The elastic component corresponds to the satellite intensity at low temperatures, and to the central peak above T_P. The inelastic response shows some softening as $T \to T_P$, as well as an increase in phonon damping. Below T_P, the spectra can be fitted assuming a single-oscillator response, as above T_P.

The spectra in figure 13(b) have been analysed using a damped harmonic oscillator response function, convoluted with the instrumental energy resolution (25 GHz fwhm). The results of the analysis are plotted in figure 14. The phonon energy decreases close to T_P and at the same time the damping increases. Below T_P one recovers the same response as above, only with a slightly reduced structure factor. We find no indication for a change in line-shape associated with a splitting of the TA response into phase and amplitude modes,

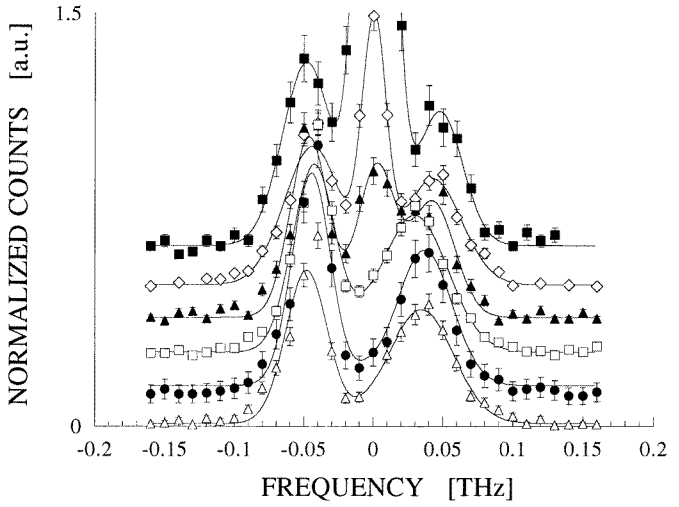

(a)

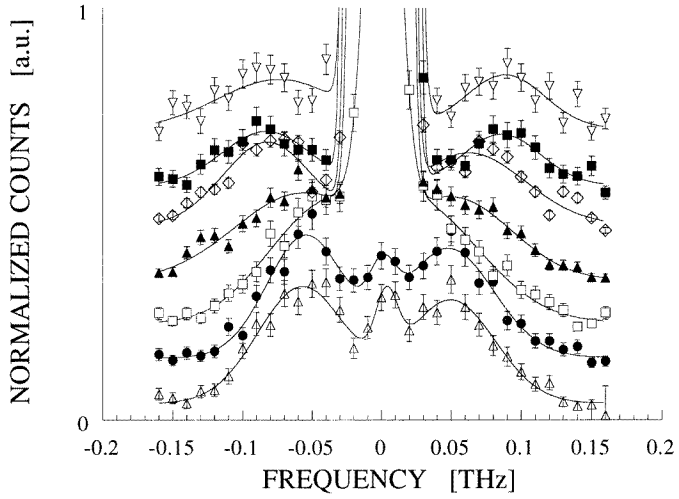

(b)

Figure 13. (a) Constant-Q scans for $(TaSe_4)_2I$, at the L point (2, 2, 4.085) below and above T_P ($T_P = 253$ K). The vertical scales are normalized using a factor proportional to the temperature, to account for the effect of varying thermal population factors. Temperatures (in K): △: 300; ●: 285; □: 270; ▲: 230; ◇: 180; ■: 100. (b) Constant-Q scans at the satellite position (the A point in figure 2) above and below T_P in $(TaSe_4)_2I$ ($T_P = 253$ K). The vertical scales are normalized using a factor proportional to T. Temperatures (in K): △: 300; ●: 285; □: 270; ▲: 230; ◇: 180; ■: 100; ▽: 50.

as would be expected for a purely displacive transition.

AC conductivity measurements below T_P reveal a sharp resonance at 30 GHz [47] in nominally pure $(TaSe_4)_2I$. The frequency and width of the resonance are found to be remarkably sensitive to dilute Nb doping. For a Nb concentration of 1.2%, the authors of reference [47] find that the position of the resonance is shifted to 120 GHz and is considerably broadened (110 GHz fwhm instead of the value 20 GHz obtained for the

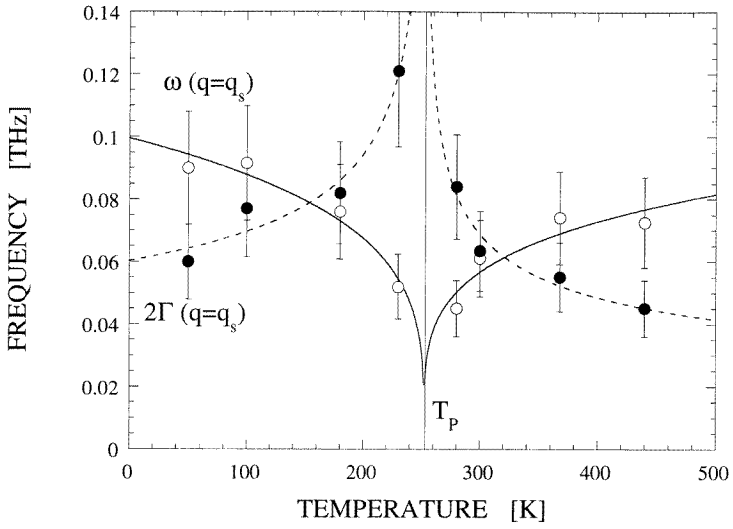

Figure 14. The temperature dependence of the TA phonon frequency and damping at the CDW satellite position in $(TaSe_4)_2I$ ($T_P = 253$ K).

pure compound). This behaviour is consistent with the interpretation of the resonance as a pinned CDW phason, for which the pinning frequency and linewidth are expected to increase together with the concentration of pinning centres [48].

These results are difficult to reconcile with our data shown in figures 13(b) and 14. A limited amount of phason–amplitudon decoupling may possibly be present in the neutron spectra taken below T_P and may go undetected due to finite frequency and wavevector resolution. This would also account for the apparent saturation of the phonon linewidth at about 60 GHz in the low-temperature neutron spectra, far above the 20 GHz linewidth of the $\sigma(\omega)$ resonance.

A more definite comparison between the two techniques could possibly be obtained in the future using doped samples, for which resolution limitations would be less severe in the neutron case. One should also keep in mind the fact that the reconstruction of the phonon spectrum below T_P, in a system characterized by an order parameter with $n = 8$ components, such as $(TaSe_4)_2I$, is likely to be considerably more complex than the simple phason–amplitudon decoupling observed in the standard $n = 2$ case. In fact, it is known from previous work on biphenyl [49] and $BaMnF_4$ [50] ($n = 4$) and on quartz [51, 52] ($n = 6$), that the number of distinct excitation frequencies to be observed near $\boldsymbol{q} = \boldsymbol{q}_s$ (i.e. phasons, amplitudons and uncondensed soft modes) will depend on the single-$\boldsymbol{q}$ or multiple-$\boldsymbol{q}$ nature of the modulated phase. Although the details have not been worked out in the $n = 8$ case, one expects all of these modes to be observable *simultaneously* by means of inelastic neutron scattering (for a large multi-domain sample), whereas only a subset of these modes should be activated in the $\sigma(\omega)$ spectra. This may well account for the difference in frequency and linewidth between the spectra obtained by the two techniques.

5. The strong-coupling model

The above measurements, together with previously reported structural and inelastic neutron scattering results, provide a comprehensive picture of the Peierls instability in $(TaSe_4)_2I$ on

the basis of which we may now return to the question addressed in section 1 concerning the nature of the electron–phonon coupling in this family of compounds.

Above T_P, strongly correlated fluctuations are observed in $(TaSe_4)_2I$. At 270 K ($T_P + 30$ K), in-plane and in-chain correlation lengths extend up to 100 Å and 180 Å, respectively. At the same relative temperature (240 K) the corresponding values for $(NbSe_4)_2I$, determined by x-ray scattering [15], are around 35 and 50 Å, respectively. Part of the difference may be related to the longer wavelength of the modulation in the Ta compound, resulting in a more pronounced 'modulated strain' character for the atomic displacements involved.

In both cases, it seems highly unlikely that such 3D correlated fluctuations could reduce T_P by a factor 2 or 3 with respect to its mean-field value. This, as well as the large amplitude of the modulated displacements, casts some doubt on the applicability of weak-coupling theory to the cases of $(TaSe_4)_2I$ and $(NbSe_4)_2I$.

In the preceding section we have attempted to characterize the low-energy excitations at and around the wavevector of the incommensurate superstructure. The only hint of a phase transition as far as the dynamics is concerned lies in the limited softening of the acoustic phonon branch close to T_P. We have not observed softening of any one of the lower-frequency optical modes, in particular the TO mode of same polarization, as initially proposed by Sugai *et al* [28].

The softening of the acoustic phonon does not have a critical character. Critical behaviour of the elastic (or unresolved quasi-elastic) central peak is observed: its intensity and correlation lengths diverge on approaching T_P. This leads us to view the Peierls transition in $(TaSe_4)_2I$ more as an ordering process than as a displacive-type instability.

Indeed, the existence of Peierls transitions with order–disorder dynamics has been predicted by Aubry and co-workers [4, 5] in the context of strong-coupling theory. Beyond a critical value k_c of the electron–phonon coupling parameter k, the ground state of the interacting electron–phonon system cannot be calculated perturbatively, starting from the unperturbed metallic state. This 'non-analytical' regime is characterized by the existence of localized electronic states (bipolarons) strongly pinned to the lattice. However, this bipolaronic state should not be confused with the bipolaronic regime referred to in the context, for instance, of high-T_c superconductors [53]. In this latter case, the bipolarons are isolated defects with small or negligible overlapping of the corresponding wavefunctions. Aubry's bipolarons form a dense ensemble which in the limit $k \to \infty$ gives rise to a bond ordering wave. The normalized electronic eigenstate of the bipolaron is given by

$$\Psi_{(x)} = \frac{k}{2\sqrt{2}} \frac{1}{\cosh(k^2 x/4)} \tag{3}$$

where the parameter k is defined as

$$k = \lambda \sqrt{\frac{2}{tM\omega_0^2}}. \tag{4}$$

ω_0 and M are the constant frequencies and masses of identical oscillators located at each lattice site, t is the electronic exchange coupling between neighbouring sites and λ is the usual dimensionless electron–phonon coupling constant.

In such a picture, the energy scale corresponding to the Peierls gap $2\Delta(0)$ is the bipolaron formation energy. This latter energy is closely related to the energy of pinning of a single bipolaron to the lattice (the Peierls–Nabarro potential E_{PN}). The activated nature of the electrical conductivity below as well as above T_P (the 'pseudo-gap') is accounted for in terms of bipolaron hopping. The Peierls transition corresponds to the ordering temperature

of the bipolaronic fluid. The order of magnitude of $k_B T_P$ is fixed by bipolaron interaction energies which, consistently, may be assumed to be much lower than the bipolaron formation energy; hence $k_B T_P \ll 2\Delta(0)$ ($2\Delta(0) = 11.4 k_B T_P$ for $(TaSe_4)_2I$).

In the strong-coupling limit, the dynamics associated with the Peierls transition is of the Ising pseudo-spin type. The discrete Ising variable corresponds to the occupation of a given lattice site by the centre of a bipolaron. The collective dynamics near T_P is expected to be relaxational, with a characteristic microscopic relaxation time proportional to $\exp\{E_{PN}/k_B T_P\}$ and thus quite long on a phonon timescale. The same applies to the CDW fluctuation spectrum below T_P.

The above predictions are in qualitative agreement with our experimental observations for pure $(TaSe_4)_2I$. Concerning the effect of doping, however, one finds it difficult to account for the strong influence of dilute isoelectronic impurities within a localized-electron framework. The primary effect of adding 1.2% Nb impurities should be to localize the conduction electron wavefunctions over chain segments with an average length of the order of the average distance between impurities along a given chain (≈800 Å). If, however, the electronic wavefunctions are *already* localized over a much smaller distance, as implied in Aubry's strong-coupling picture, one would not expect impurities to play such a major role.

To summarize, the strong-coupling model may account for:

(i) the large ratio between the low-temperature Peierls gap $2\Delta(0)$ and the transition temperature T_P;
(ii) the large amplitude (≈0.1 Å) of the low-temperature ionic modulation;
(iii) the order–disorder character of the pre-transitional fluctuations.

On the other hand it does *not* account for:

(i) the nearly isotropic character of the pre-transitional fluctuations;
(ii) the large 'transverse acoustic' component of the ionic modulation;
(iii) the strong influence of isoelectronic doping on the modulation periodicity.

In order to understand these latter aspects, which are *specific* to the case of $(TaSe_4)_2I$, one needs to take explicit account of the fact that, in this case, the Peierls instability is a zone-centre ($\boldsymbol{q} \approx 0$) instability (see section 2). This *specific* aspect of $(TaSe_4)_2I$ (and $(NbSe_4)_2I$) implies that the standard Fröhlich description of the interacting electron–phonon system must be reformulated. Since conduction electrons are not expected to couple *directly* to long-wavelength transverse acoustic modes, one must assume that they couple to specific optical-like deformations which in turn interact with the long-wavelength acoustic degrees of freedom. A proper description of the instability should therefore include the acoustic variables as well as the electron-coupled optical variables. The low-temperature modulated distortion, which is the end result of this two-stage interaction process, should have a mixed optical–acoustic character, even though, experimentally, the acoustic component appears to be dominant.

6. Strain coupling: a Landau–Ginzburg model

The object of this section is threefold:

(i) to identify the nature and symmetry of the optical variables which couple directly to the conduction electron CDW;
(ii) to construct a free-energy functional expressed in terms of these optical variables as well as the acoustic variables;

(iii) to derive the characteristics of the CDW ground state by minimization of the free-energy functional.

Following the band calculation of Gressier *et al* [23], we assume a quarter-filled Ta d_{z^2} conduction band with strong one-dimensional character. The optical modes which couple to the CDW fluctuations must then involve tetramerization-like deformations of the –Ta–Ta– chains, with Ta displacements along $\boldsymbol{c}$ [23]. The Se^{2-} dimers which are covalently bonded to the Ta ions are expected to readjust to the Ta displacements. However, because of the weak interchain bonding, we may view these tetramerization modes as *intrachain* modes, with only weak dispersion in the directions normal to the chains.

Far above T_P, we thus expect a one-dimensional fluctuation regime, where CDW fluctuations on adjacent chains are only weakly correlated. This regime should give rise to a planar distribution of x-ray diffuse scattering, corresponding to integer values of l ($\boldsymbol{Q} = h\boldsymbol{a}^* + k\boldsymbol{b}^* + l\boldsymbol{c}^*$). One should note that, in practice, this regime may be quite difficult to detect because of the highly anisotropic dispersion of the TA branch polarized along $\boldsymbol{c}$ (see section 4.1) which gives rise to a similar set of diffuse scattering sheets, also for integer l-values.

As the temperature is lowered, transverse antiphase CDW correlations develop as a result of interchain interactions and Coulomb interactions between fluctuating CDWs on adjacent chains. As a result, the diffuse scattering intensity associated with the optical-mode displacements should concentrate around crystallographic Γ points ($\boldsymbol{q}_s \approx 0$). In that (3D) regime, *gradient* interaction terms between optical and acoustic degrees of freedom become important. They give rise to two effects:

(i) the fluctuating displacements acquire a strong acoustic component which in the present case appears to be dominant, at least below room temperature;

(ii) the critical fluctuations concentrate around positions (i.e. the satellite positions) which are close to but distinct from the Γ point.

In the present model, the values of the satellite wavevector components are not related to the topology of the conduction electron Fermi surface. They are determined by the strength of the gradient interaction terms. Similar phenomenological models have been developed in the context of incommensurate long-wavelength-modulated dielectrics, such as quartz [54], sodium nitrite and thiourea [55]. In these materials the incommensurate structure arises from the presence of a pseudo-Lifshitz invariant involving an optical order parameter and the elastic deformations. The present model is also related to the TA–TO coupled-mode model of Sugai *et al* [28], except that the TA and TO modes which are coupled here have quite different polarizations and are not related via a zone-folding operation, as postulated in [28].

Table 1. The character table for the 422 (D_4) point group of $(TaSe_4)_2I$.

	$E(h_1)$ (x, y, z)	$C_{2x}(h_2)$ $(x, \bar{y}, \bar{z})$	$C_{2y}(h_3)$ $(\bar{x}, y, \bar{z})$	$C_{2z}(h_4)$ $(\bar{x}, \bar{y}, z)$	$C_{2\bar{x}y}(h_{13})$ $(\bar{y}, \bar{x}, \bar{z})$	$C_{4z}(h_{14})$ $(\bar{y}, x, z)$	$C_{4\bar{z}}(h_{15})$ $(y, \bar{x}, z)$	$C_{2xy}(h_{16})$ $(y, x, \bar{z})$		
A_1	1	1	1	1	1	1	1	1		$x^2 + y^2, z^2$
A_2	1	$\bar{1}$	$\bar{1}$	1	$\bar{1}$	1	1	$\bar{1}$	z, R_z	
B_1	1	1	1	1	$\bar{1}$	$\bar{1}$	$\bar{1}$	$\bar{1}$		$x^2 - y^2$
B_2	1	$\bar{1}$	$\bar{1}$	1	1	$\bar{1}$	$\bar{1}$	1		xy
E	$\begin{pmatrix} 1 & 0 \\ 0 & 1 \end{pmatrix}$	$\begin{pmatrix} 0 & 1 \\ 1 & 0 \end{pmatrix}$	$\begin{pmatrix} 0 & \bar{1} \\ \bar{1} & 0 \end{pmatrix}$	$\begin{pmatrix} \bar{1} & 0 \\ 0 & \bar{1} \end{pmatrix}$	$\begin{pmatrix} 0 & \bar{1} \\ 1 & 0 \end{pmatrix}$	$\begin{pmatrix} i & 0 \\ 0 & \bar{i} \end{pmatrix}$	$\begin{pmatrix} \bar{i} & 0 \\ 0 & i \end{pmatrix}$	$\begin{pmatrix} 0 & i \\ \bar{i} & 0 \end{pmatrix}$	$(x, y)(R_x, R_y)$	(xz, yz)

Before continuing our discussion it is necessary to determine the symmetry of the zone-centre mode involved in the Ta tetramerization. The site symmetry for Ta(1) atoms (figure 1 in reference [17]) is orthorhombic $2_{(\|c)}2_{(\|a)}2_{(\|b)}$ and the Ta(1)–Se near-neighbour distances are 2.623 Å and 2.689 Å. The site symmetry for Ta(2) atoms is also orthorhombic $2_{(\|c)}2_{(\|(a+b))}2_{(\|(a-b))}$ and the corresponding distances are 2.600 Å and 2.713 Å. The main distinction between the two Ta sites comes from the iodine positions which are closer to Ta(1) than to Ta(2)—leading to the +5 and +4 formal valence states, respectively.

For a Bravais group 422 (or D_4) we have five irreducible representations (IR), four one-dimensional (A_1, A_2, B_1 and B_2) representations and one bidimensional (E) one, whose characters are presented in table 1. The decomposition of modes in IR is

$$7A_1 \oplus 9A_2 \oplus 7B_1 \oplus 7B_2 \oplus 18E.$$

Note that the IR decomposition in [42] is incorrect because it is based on four formula units per unit cell, whereas the *primitive* unit cell contains only two.

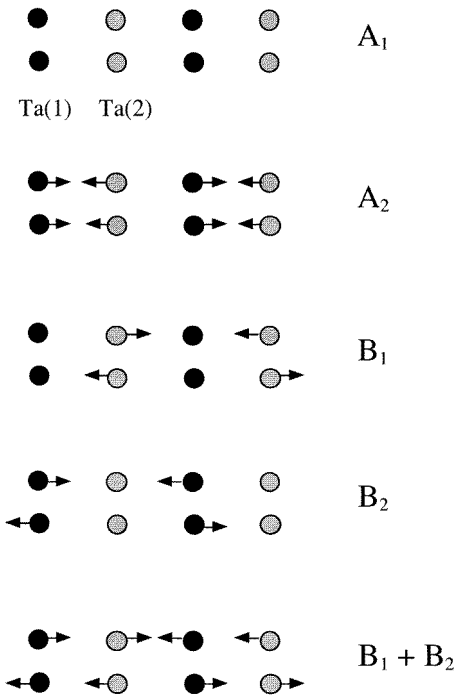

Figure 15. $(TaSe_4)_2I$: the metal-atom displacement pattern for different zone-centre irreducible representations. Different types of Ta tetramerization are labelled as B_1, B_2, $B_1 + B_2$.

The Ta displacement vectors are shown in figure 15 and are as follows.

(i) In the A_1 representation, none of the Ta atoms move.

(ii) In the A_2 representation, Ta(1) and Ta(2) atoms move in opposite directions, and dimers can be formed.

(iii) Only Ta(1) atoms move in the B_1 representation, leading to the formation of Ta(2)–Ta(1)–Ta(2) trimers and Ta(1) monomers.

(iv) Conversely, only Ta(2) atoms move in the B_2 representation, leading to the formation of Ta(1)–Ta(2)–Ta(1) trimers and Ta(2) monomers.

(v) Finally, in the doubly degenerate E representation, the Ta(1) and Ta(2) motions are confined to the basal plane.

It is easy to see that tetramers are obtained by combining B_1 and B_2 as shown at the bottom of figure 15. Furthermore, one may verify that the resulting modulations on neighbouring chains are 'π-out-of-phase'. The peculiarity of the modes in this space group is that B_1 and B_2 belong to the same IR of the 'little group' for wavevectors $\boldsymbol{q}$ along $\boldsymbol{c}^*$ and to different IR for $\boldsymbol{q}$ along high-symmetry directions in the basal plane (even and odd, respectively, with respect to the C_{2x} (or C_{2y}) symmetry operations, and odd and even with respect to C_{2xy} (or $C_{2\bar{x}y}$)).

Table 2. The transformation table for the order parameters η_1 and η_2 and their gradients, and for the shear elastic strains (e_4, e_5 and e_6). Note from table 1 that e_6 transforms as η_2 and $e_1 - e_2$ as η_1.

	$\begin{pmatrix}\eta_2\\ e_6\end{pmatrix}$	$\begin{pmatrix}\eta_1\\ e_1-e_2\end{pmatrix}$	e_4	e_5	x	y	z
C_{4z}	$-\eta_2$	$-\eta_1$	e_5	$-e_4$	$-y$	x	z
C_{2z}	η_2	η_1	$-e_4$	$-e_5$	$-x$	$-y$	z
C_{2x}	$-\eta_2$	η_1	e_4	$-e_5$	x	$-y$	$-z$
C_{2y}	$-\eta_2$	η_1	$-e_5$	$-e_4$	y	x	$-z$

As Ta(1) and Ta(2) sites are crystallographically very similar, one expects the B_1 and B_2 eigenfrequencies to be nearly equal. In a Landau–Ginzburg free-energy expansion, it is therefore necessary to include both types of displacement, i.e. the lowest-frequency B_1 mode (η_1) and the lowest-frequency B_2 mode (η_2) as potential order parameters with nearly degenerate moduli. Making use of table 2, we construct the second-order invariants involving η_1, η_2 and their derivatives and the corresponding strain interaction terms.

The Landau free-energy density is written as a sum of all possible lowest-order invariants:

$$F(\boldsymbol{r}) = F_\eta(\boldsymbol{r}) + F_E(\boldsymbol{r}) + F_C(\boldsymbol{r}) \tag{5}$$

with

$$\begin{aligned} F_\eta = {} & \alpha_1\eta_1^2 + \alpha_2\eta_2^2 + \beta_1\eta_1^4 + \beta_2\eta_2^4 + \beta_3\eta_1^2\eta_2^2 + f\left(\eta_2\frac{\partial\eta_1}{\partial z} - \eta_1\frac{\partial\eta_2}{\partial z}\right) \\ & + \tau_{11}\left[\left(\frac{\partial\eta_1}{\partial x}\right)^2 + \left(\frac{\partial\eta_1}{\partial y}\right)^2\right] + \tau_{21}\left[\left(\frac{\partial\eta_2}{\partial x}\right)^2 + \left(\frac{\partial\eta_2}{\partial y}\right)^2\right] \\ & + \tau_{12}\left(\frac{\partial\eta_1}{\partial z}\right)^2 + \tau_{22}\left(\frac{\partial\eta_2}{\partial z}\right)^2 \end{aligned} \tag{6a}$$

$$F_E = \frac{1}{2}C_{11}(e_1^2 + e_2^2) + \frac{1}{2}C_{33}e_3^2 + C_{12}e_1e_2 + C_{13}(e_1 + e_2)e_3 + \frac{1}{2}C_{44}(e_4^2 + e_5^2) + \frac{1}{2}C_{66}e_6^2 \tag{6b}$$

$$F_C = \delta_1\eta_1(e_1 - e_2) + \delta_2\eta_2e_6 + \gamma_1\left(e_5\frac{\partial\eta_1}{\partial y} + e_4\frac{\partial\eta_1}{\partial x}\right) + \gamma_2\left(e_5\frac{\partial\eta_2}{\partial x} - e_4\frac{\partial\eta_2}{\partial y}\right). \tag{6c}$$

To discuss the stability of the modulated ground state, it is useful to introduce the acoustic displacement vector $\boldsymbol{u}(\boldsymbol{r}) = (u_1(\boldsymbol{r}), u_2(\boldsymbol{r}), u_3(\boldsymbol{r}))$ related to the elastic

deformations through

$$\begin{aligned} e_1 = u_{11} &= \frac{\partial u_1}{\partial x} \qquad & e_4 = u_{23} &= \frac{1}{2}\left(\frac{\partial u_2}{\partial z} + \frac{\partial u_3}{\partial y}\right) \\ e_2 = u_{22} &= \frac{\partial u_2}{\partial y} \qquad & e_5 = u_{13} &= \frac{1}{2}\left(\frac{\partial u_1}{\partial z} + \frac{\partial u_3}{\partial x}\right) \\ e_3 = u_{33} &= \frac{\partial u_3}{\partial z} \qquad & e_6 = u_{12} &= \frac{1}{2}\left(\frac{\partial u_1}{\partial y} + \frac{\partial u_2}{\partial x}\right). \end{aligned} \tag{7}$$

We introduce the Fourier components of the variables $\eta_1(\boldsymbol{r})$, $\eta_2(\boldsymbol{r})$ and $\boldsymbol{u}(\boldsymbol{r})$:

$$\begin{aligned} \eta_j(\boldsymbol{r}) &= \sum_{\boldsymbol{q}} \eta_{j\boldsymbol{q}} \mathrm{e}^{\mathrm{i}\boldsymbol{q}\cdot\boldsymbol{r}} \qquad \text{for } j = 1, 2 \text{ and } \eta_{j-\boldsymbol{q}} = \eta^*_{j\boldsymbol{q}} \\ u_{ij}(\boldsymbol{r}) &= \epsilon_{ij} + \frac{\mathrm{i}}{2}\sum_{\boldsymbol{q}\neq 0}(q_i u_{j\boldsymbol{q}} + q_j u_{i\boldsymbol{q}})\mathrm{e}^{\mathrm{i}\boldsymbol{q}\cdot\boldsymbol{r}}. \end{aligned} \tag{8}$$

The thermodynamical potential is then given by

$$\Phi = \int F(\boldsymbol{r})\ \mathrm{d}\boldsymbol{r} = V\sum_{\boldsymbol{q}} \Phi_{\boldsymbol{q}}. \tag{9}$$

In order to simplify the expression for the potential $\Phi_{\boldsymbol{q}}$, one must examine the values of the relative phases of the complex variables η_{1q}, η_{2q} and $\boldsymbol{u}_q$. These phases are determined in first order by the following three coupling terms:

$$f\left(\eta_2\frac{\partial\eta_1}{\partial z} - \eta_1\frac{\partial\eta_2}{\partial z}\right) \to -\mathrm{i}q_3 f(\eta^*_{1q}\eta_{2q} - \eta_{1q}\eta^*_{2q}) \tag{10}$$

$$\eta_1(e_1 - e_2) \to \frac{\mathrm{i}}{2}\eta^*_{1q}(q_1u_{1q} - q_2u_{2q}) - \frac{\mathrm{i}}{2}\eta_{1q}(q_1u^*_{1q} - q_2u^*_{2q}) \tag{11}$$

$$\eta_2 e_6 \to \frac{\mathrm{i}}{4}q_1(\eta^*_{2q}u_{2q} - \eta_{2q}u^*_{2q}) + \frac{\mathrm{i}}{4}q_2(\eta^*_{2q}u_{1q} - \eta_{2q}u^*_{1q}). \tag{12}$$

The first term induces a phase shift of $\pi/2$ between the variables η_{1q} and η_{2q}. In what follows, we choose the origin in such a way that η_{1q} is real:

$$\eta_{1q} = \eta^*_{1q} = \bar{\eta}_1. \tag{13}$$

Equation (10) implies that the variable η_{2q} is purely imaginary. If we assume real values for the variables u_{1q} and u_{2q}, we see that expression (11) vanishes. A finite value of η_{2q} will thus induce (see expression (12)) a modulated shear of e_6 type. In contrast, if the variables u_{1q} and u_{2q} are assumed to be imaginary, expression (12) vanishes and expression (11) will induce a modulated shear of $e_1 - e_2$ type.

This latter solution corresponds to the actual experimental situation: the atomic displacements in the CDW phase have a strong transverse acoustic component $\boldsymbol{q}(1\ 1\ 0), \boldsymbol{u}(1\ \bar{1}\ 0)$, i.e. $q_1 = q_2$, $u_{1q} = -u_{2q}$. Therefore in what follows we assume imaginary values for the variables u_{1q} and u_{2q}. This choice is not strictly valid. Normally the phases of the variables η_{2q}, u_{1q} and u_{2q} should be obtained through the simultaneous minimization of the three coupling terms (expressions (10), (11), (12)). The corresponding phase and displacement variables will then assume more general values. However, the observed satellite intensities [25] suggest that the real atomic displacements are close to the simplified solution that we consider here.

Within the above approximation we have

$$\eta^*_{2q} = -\eta_{2q} = \mathrm{i}\bar{\eta}_2 \qquad u^*_{1q} = -u_{1q} = \mathrm{i}\bar{u}_1 \qquad u^*_{2q} = -u_{2q} = \mathrm{i}\bar{u}_2. \tag{14}$$

The three terms in equation (6*c*) become

$$\eta_1(e_1 - e_2) \rightarrow \bar{\eta}_1(q_1\bar{u}_1 - q_2\bar{u}_2) \tag{15}$$

$$e_5\frac{\partial\eta_1}{\partial y} + e_4\frac{\partial\eta_1}{\partial x} \rightarrow \frac{1}{2}\bar{\eta}_1 q_1 q_2(u_{3q} + u^*_{3q}) \tag{16}$$

$$e_5\frac{\partial\eta_2}{\partial x} - e_4\frac{\partial\eta_2}{\partial y} \rightarrow \frac{\mathrm{i}}{4}\bar{\eta}_2(q_1^2 - q_2^2)(u_{3q} - u^*_{3q}) + \frac{1}{2}\bar{\eta}_2 q_3(q_1\bar{u}_1 - q_2\bar{u}_2). \tag{17}$$

The symmetry of the above expressions implies that $|q_1| = |q_2|$ and $|\bar{u}_1| = |\bar{u}_2|$, and in agreement with the experiment we choose $q_1 = q_2 = q$ and $\bar{u}_1 = -\bar{u}_2 = u$. The phase of the variable u_{3q} is then determined through equation (16):

$$u_{3q} = u^*_{3q} = u_3. \tag{18}$$

The thermodynamical potential Φ_q consists of three terms:

$$\Phi^\eta_q = \alpha_1\bar{\eta}_1^2 + \alpha_2\bar{\eta}_2^2 + 2q_3 f\bar{\eta}_1\bar{\eta}_2 + q_3^2(\tau_{12}\bar{\eta}_1^2 + \tau_{22}\bar{\eta}_2^2) + 2q^2(\tau_{11}\bar{\eta}_1^2 + \tau_{21}\bar{\eta}_2^2) + \mathrm{O}(\eta^4) \tag{19}$$

$$\Phi^E_q = C_{11}q^2u^2 + \frac{1}{2}C_{33}q_3^2u_3^2 - C_{12}q^2u^2 + \frac{1}{4}C_{44}(q^2u_3^2 + q_3^2u^2) + \frac{1}{8}C_{66}q^2u^2 \tag{20}$$

$$\Phi^C_q = 2\delta_1\bar{\eta}_1 qu + \gamma_1\bar{\eta}_1 q^2u_3 + \gamma_2\bar{\eta}_2 q_3 qu. \tag{21}$$

By minimizing $\Phi^E_q + \Phi^C_q$ with respect to u and u_3, we obtain the equilibrium values of the acoustic displacements:

$$u = -\frac{4\delta_1\bar{\eta}_1 q + 2\gamma_2\bar{\eta}_2 q q_3}{4Cq^2 + C_{44}q_3^2} \qquad u_3 = -\frac{2\gamma_1\bar{\eta}_1 q^2}{2C_{33}q_3^2 + C_{44}q^2} \tag{22}$$

with $C = C_{11} - C_{12} + \frac{1}{8}C_{66}$.

The contribution of the γ_2-term is of higher order in q_3 and thus can be neglected. Whence

$$uq = -\frac{4\delta_1\bar{\eta}_1}{4C + C_{44}\rho^2} \qquad u_3 = -\frac{2\gamma_1\bar{\eta}_1}{2C_{33}\rho^2 + C_{44}} \qquad \text{with } \rho = \frac{q_3}{q}. \tag{23}$$

Inserting equation (23) in the expression for the potential, one gets

$$\begin{aligned}
&\Phi_q = \bar{\alpha}_1\bar{\eta}_1^2 + \bar{\alpha}_2\bar{\eta}_2^2 + 2q_3 f'\bar{\eta}_1\bar{\eta}_2 + \mathrm{O}(\eta^4)\\
&\bar{\alpha}_1 = \alpha_1 + \tau_{12}q_3^2 + 2\tau_{11}q^2 - \frac{4\delta_1^2}{4C + C_{44}\rho^2} - \frac{\gamma_1^2 q^2}{C_{44} + 2C_{33}\rho^2}\\
&\bar{\alpha}_2 = \alpha_2 + \tau_{22}q_3^2 + 2\tau_{21}q^2\\
&f' = f - \frac{2\delta_1\gamma_2}{4C + C_{44}\rho^2}.
\end{aligned} \tag{24}$$

Minimizing Φ_q with respect to $\bar{\eta}_1$ and $\bar{\eta}_2$, one obtains the trivial solution $\bar{\eta}_1 = \bar{\eta}_2 = 0$ unless $\bar{\alpha}_1\bar{\alpha}_2 = q_3^2 f'^2$. To leading order in the variables q and q_3, this condition yields

$$\alpha'_1\alpha_2 + q^2\left\{2\alpha'_1\tau_{21} + 2\alpha_2\tau_{11} - \frac{\alpha_2\gamma_1^2}{C_{44} + 2C_{33}\rho^2}\right\} + q_3^2\left\{\alpha'_1\tau_{22} + \alpha_2\tau_{12} - f'^2\right\} + \mathrm{O}(q^4, q_3^4) = 0 \tag{25}$$

where α'_1 is the renormalized modulus associated with the variable η_1:

$$\alpha'_1 = \alpha_1 - \frac{4\delta_1^2}{4C + C_{44}\rho^2}. \tag{26}$$

As a result of coupling to the elastic strains, the modulus $\bar{\alpha}_1(q_1, q_3)$ acquires a non-analytic character in the small-wavevector limit:

$$\begin{aligned} \lim_{(q\to 0;q_3=0)} \bar{\alpha}_1 &= \alpha_1 - \delta_1^2/C \\ \lim_{(q=0;q_3\to 0)} \bar{\alpha}_1 &= \alpha_1. \end{aligned} \tag{27}$$

We make the assumption, consistent with the strong acoustic character of the modulated displacements, that the coupling coefficient, δ_1, of the variable η_1 and the strain $e_1 - e_2$ is large. In particular we expect the renormalization of the η_1-modulus, α_1, to be a large effect which effectively *triggers* the instability. For the sake of definiteness, we may assume that all of the coefficients appearing in the free energy (6) are temperature independent with the exception of δ_1. If $|\delta_1(T)|$ increases on cooling, the high-temperature phase becomes unstable against a *homogeneous* distortion at a temperature such that

$$\alpha_1'(\rho = 0, T) = \alpha_1 - \delta_1^2(T)/C = 0. \tag{28}$$

The important information contained in equation (25) is the fact that the instability condition may be achieved while the leading term, $\alpha_1'\alpha_2$, is still weakly positive. For this to occur, it is sufficient that the coefficient of the q_3^2-term be negative:

$$\alpha_1'\tau_{22} + \alpha_2\tau_{12} - f'^2 < 0. \tag{29}$$

This guarantees that, on cooling, the instability will first be achieved for some finite value of q_3. Through the ρ-dependence of α_1', this will in turn entail the in-plane wavevector component q having a finite value. Although this is not essential, one may note that the coefficient of the q^2-term in equation (25) may itself be negative:

$$2\alpha_1'\tau_{21} + 2\alpha_2'\tau_{11} - \alpha_2\gamma_1^2/(C_{44} + 2C_{33}\rho^2) < 0. \tag{30}$$

The coefficients τ_{11} and τ_{21} correspond to the in-plane dispersion coefficients for the tetramerization modes: due to the weak *interchain* interactions, these *intrachain* modes are expected to be essentially dispersionless in the x–y plane ($\tau_{11} \approx \tau_{21} \approx 0$), in which case condition (30) is readily fulfilled.

The equilibrium values of the modulation wavevector components (q, q, q_3) may in principle be obtained from the minimization of the lhs of equation (25) with respect to q and q_3. This procedure is however beyond the scope of the present work, since it would involve writing down explicit expressions for the fourth- and higher-order terms in equation (25), terms for which we have little experimental input. One may simply note that the small values of q and q_3 found experimentally imply large, positive values for the fourth-order coefficients. This is also consistent with the overall picture of the instability as a 'zone-centre' Peierls transition ($2k_F = 0$), for which the finite value of the modulation wavevector arises from gradient interaction terms and through the (indirect) coupling of the electronic variables to the elastic strains.

7. Discussion

The model presented above is incomplete and, clearly, oversimplified. It nevertheless provides a plausible interpretation for a number of unusual aspects of the Peierls instability in $(TaSe_4)_2I$.

(i) The transverse acoustic character of the modulated displacements below T_P is explained via the bi-linear coupling between the η_1 optical-mode distortion and the $e_1 - e_2$ shear strain.

(ii) The finite value of the in-plane CDW wavevector component is accounted for via the same mechanism.

(iii) The finite value of the CDW wavevector component along the chains is accounted for via a gradient interaction ('pseudo-Lifshitz-invariant') term for the two nearly degenerate Ta-tetramerization modes.

(iv) In principle, the values of the CDW wavevector components could also be connected to the Fermi surface nesting topology. The sensitivity of these values to dilute isoelectronic doping is in that case difficult to rationalize. In the present model the equilibrium values of q and q_3 result from a balance between several competing free-energy terms. In such a case a small change in one of the terms can have a large effect. For instance, the inclusion of $\approx$1% Nb impurities may affect the long-wavelength dispersion of the tetramerization modes (via changes in the electron–phonon coupling strength) and/or the strength of their interaction with the elastic strains.

On the other hand, the model in its present state is not sufficiently refined for predicting the equilibrium values of the CDW wavevector components. An even more difficult task would be to reproduce the temperature evolution of these components and to predict the occurrence or non-occurrence of a low-temperature commensurate phase with $q = q_3 = 0$. Experimentally, q and q_3 are found to be temperature independent, within the accuracy of the measurements, and no lock-in phase is observed. It is not clear however whether or not such a simple behaviour can be reproduced within the present framework.

A more basic objection to the present model has to do with the fact that the Ta-tetramerization modes have not been identified experimentally so far. Although both modes should be observable by means of Raman and inelastic neutron scattering, the eigenfrequencies associated with the moduli α_1 and α_2:

$$\omega_{1,2} = (2\alpha_{1,2})^{1/2} \qquad (T > T_P) \tag{31}$$

are still unknown. In the remainder of this section we shall examine this point in more detail.

The B_1 and B_2 modes are Raman active in (a, a) and (a, b) polarization, respectively. From the data of Sugai *et al* [28], the lowest-frequency modes are located at about 70 cm^{-1} ($\approx$2 THz), in both geometries. None of them, however, exhibits any marked temperature dependence. This is in fact a general feature of the Raman spectra for $(TaSe_4)_2I$: even the 93 cm^{-1} mode observed in (c, c) geometry, which the authors of reference [28] tentatively identify as the CDW-coupled optical mode, only shows a minute frequency shift at around T_P.

In the framework of the present model one does not expect the temperature renormalization of the η_1-modulus to be observable by means of Raman or inelastic neutron scattering. The reason is twofold.

(i) The relationship (31) between modulus and eigenfrequency holds only in the displacive limit. In the general case, α_1 and α_2 have the dimensions of inverse static susceptibilities associated with the variables η_1 and η_2. Through the Kramers–Krönig and fluctuation-dissipation theorems, α_1 and α_2 are related to the frequency-integrated response of the variables η_1 and η_2. In the order–disorder limit the important part of the response is relaxational and corresponds to processes of correlated jump diffusion between equivalent configurations or potential wells. The phonon frequency in that case is only the high-frequency part of the response, corresponding to oscillations around a particular configuration or potential well. It is relatively insensitive to the temperature-dependent ordering process associated with the phase transition.

(ii) Even if the high-temperature dynamical response of the variable η_1 is strictly phonon-like, the renormalization of α_1 due to the coupling to the elastic strains (equation (26)) will give rise to order–disorder dynamics. The reason for this is simply that the η_1-fluctuations occur on a very short timescale (in the THz range) while strain fluctuations are slow. In an inelastic scattering experiment therefore, the η_1-vibration will be elastically clamped and occur at the 'bare' frequency $(2\alpha_1)^{1/2}$. In that case nothing distinguishes the η_1-mode from an ordinary optical mode.

The above remarks apply directly to Raman scattering and, in the long-wavelength limit, to inelastic neutron scattering as well. In the case of neutron scattering one should also take into account the fact that most of the experiments have been carried out near strong Bragg reflections of the type $(h\ k\ l)$ with $h+k=2n$. This is also where the strong satellite reflections are observed. One can readily show that the Ta-tetramerization modes are extinct near $h+k=2n$. In practice they may still be observable because of the accompanying Se displacements, but probably only weakly so.

8. Conclusions

In this paper we have studied the Peierls phase transition in the quasi-one-dimensional charge-density-wave compound $(TaSe_4)_2I$ by elastic and inelastic neutron scattering techniques. Our elastic neutron scattering experiments have shown that this compound exhibits different features to the rest of the known materials undergoing Peierls transitions: nearly isotropic correlation lengths for the fluctuations above T_P, acoustic-like character of the corresponding atomic displacements and variation of the incommensurate wavevector on doping with isoelectronic impurities (Nb). We have shown that we can understand most of these features within the framework of a semi-phenomenological Landau–Ginzburg model. A strong coupling between the conduction electrons and the Ta-tetramerization mode, together with a temperature-dependent coupling between the latter modes and the elastic strains, may lie at the origin of the phase transition in this compound.

The results from our inelastic neutron scattering experiments have shown the absence of a clear soft-phonon-mode behaviour at the phase transition and the presence of a central peak whose intensity diverges at T_P. This indicates that the phase transition in $(TaSe_4)_2I$ falls in the class of order–disorder transitions, as predicted by strong-coupling theories [4, 5].

Acknowledgments

We are very happy to thank P Boutrouille and A Brochier for their kind assistance during the experiments, J Chen for the resistivity measurements and M Saint-Paul for communicating his ultrasound results prior to publication. One of us, JEL, also acknowledges financial support from the Spanish Ministry of Education and Science.

References

[1] See, for reviews on CDW systems,
Monceau P 1985 *Electronic Properties of Quasi-One-Dimensional Conductors* Parts I and II, ed P Monceau (Dordrecht: Reidel)
Grüner G 1988 *Rev. Mod. Phys.* **60** 1129
Grüner G 1994 *Density Waves in Solids* (Reading: Addison-Wesley)
Gorkov L P and Grüner G (ed) 1989 *Charge Density Waves in Solids (Modern Problems in Condensed Matter Sciences 25)* (New York: Elsevier)

Schlenker C (ed) 1989 *Low-Dimensional Properties of Molybdenum Bronzes and Oxides* (Dordrecht: Kluwer Academic)
Brazovskii S and Monceau P (ed) 1993 *Proc. Int. Workshop on Electronic Crystals; J. Physique Coll.* IV **2**
Schlenker C, Dumas J, Greenblatt M and Van Smaalen S 1996 *Physics and Chemistry of Low-Dimensional Inorganic Conductors (NATO ASI Series B: Physics, vol 354)* (New York: Plenum)
[2] Tutto I and Zawadowski A 1985 *Phys. Rev.* B **32** 2449
[3] Lee P A, Rice T M and Anderson P W 1973 *Phys. Rev. Lett.* **31** 462
[4] Aubry S and Quemerais P 1989 *Low-Dimensional Properties of Molybdenum Bronzes and Oxides* ed C Schlenker (Dordrecht: Kluwer Academic) p 295
[5] Aubry S, Abramovici G and Raimbault J L 1992 *J. Stat. Phys.* **67** 675
[6] Pouget J P and Comes R 1989 *Charge Density Waves in Solids (Modern Problems in Condensed Matter Sciences 25)* ed L P Gorkov and G Grüner (New York: Elsevier) p 85
[7] Johnston D C 1984 *Phys. Rev. Lett* **52** 2049
[8] Travaglini G, Wachter P, Marcus J and Schlenker C 1981 *Solid State Commun.* **37** 599
[9] Pouget J P, Noguera C, Moudden A H and Moret R 1985 *J. Physique* **46** 1731 (erratum 1986 **47** 145)
[10] Girault S, Moudden A H and Pouget J P 1989 *Phys. Rev.* B **39** 4430
[11] Varma C M and Simons A L 1983 *Phys. Rev. Lett.* **51** 138
[12] Wang Z Z, Saint-Lager M C, Monceau P, Renard M, Gressier P, Meerschaut A, Guemas L and Rouxel J 1983 *Solid State Commun.* **46** 325
[13] Maki M, Kaiser M, Zettl A and Grüner G 1983 *Solid State Commun.* **46** 497
[14] Berner D, Scheiber G, Gaymann A, Geserich H, Monceau P and Levy F 1993 *Proc. Int. Workshop on Electronic Crystals; J. Physique Coll.* IV **2** 255
[15] Fujishita H, Sato M and Hoshino S 1984 *Solid State Commun.* **49** 313
Fujishita H, Sato M, Sato S and Hoshino S 1985 *J. Phys. C: Solid State Phys.* **18** 1105
[16] Saint-Paul M, Monceau P and Levy F 1988 *Solid State Commun.* **67** 581
[17] Gressier P, Guemas L and Meerschaut A 1982 *Acta Crystallogr.* B **28** 2877
[18] Roucau C, Ayroles R, Gressier P and Meerschaut A 1984 *J. Phys. C: Solid State Phys.* **17** 2993
[19] Kikkawa S, Venosono S and Koizumi M 1983 *Proc. Int. Symp. on Non-Linear Transport and Related Phenomena in Inorganic Quasi-One-Dimensional Conductors (Sapporo)* (Sapporo: Hokkaido University) p 245
[20] Sato E, Ohtake K, Yamamoto R, Doyama M, Mori T, Soda K, Suga S and Endo K 1985 *Solid State Commun.* **55** 1049
[21] Forro L, Cooper J R, Janossy A and Maki M 1987 *Solid State Commun.* **62** 715
[22] Bansal C and Surendranath K 1990 *Solid State Commun.* **76** 209
[23] Gressier P, Wangbo M H, Meerschaut A and Rouxel J 1984 *Inorg. Chem.* **23** 1221
[24] Geserich H P, Scheiber G, Dürrer M, Levy F and Monceau P 1986 *Physica* B **143** 198
[25] Lee K B, Davidov D and Heeger A J 1985 *Solid State Commun.* **54** 673
[26] Fujishita H, Shapiro S M, Sato M and Hoshino S 1986 *J. Phys. C: Solid State Phys.* **19** 3049
[27] Monceau P, Bernard L, Currat R, Levy F and Rouxel J 1986 *Physica* B **136** 352
Monceau P, Bernard L, Currat R, Levy F and Rouxel J 1987 *Synth. Met.* **19** 819
[28] Sugai S, Sato M and Kurihara S 1985 *Phys. Rev.* B **32** 6809
[29] Lorenzo J E, Currat R, Monceau P, Hennion B and Levy F 1993 *Phys. Rev.* B **47** 10 116
[30] Brezin E, LeGuillou J C and Zinn-Justin J 1994 *Phys. Rev.* B **10** 892
[31] Mukamel D and Krinsky S 1976 *Phys. Rev.* B **13** 5065
[32] Requardt H, Kalning M, Burandt B, Press W and Currat R 1996 *J. Phys.: Condens. Matter* **8** 2327
[33] Lorenzo J E, Thurston R, Currat R, Monceau P, Favre-Nicolin V, Requardt H and Hodeau J L 1997 unpublished
[34] See, for instance, table 3 in reference [6].
[35] Saint-Paul M, Holtmeier S, Britel R, Monceau P, Currat R and Levy F 1996 *J. Phys.: Condens. Matter* **8** 2021
[36] Monceau P, Bernard L, Currat R and Levy F 1989 *Physica* B **156+157** 20
[37] Stockmayer W H and Hecht C E 1953 *J. Chem. Phys.* **21** 1954 and references therein
[38] Nicklow R, Wakabayashi N and Smith H G 1972 *Phys. Rev.* B **5** 4951
[39] Lorenzo J E, Currat R, Dianoux A J, Monceau P and Levy F 1996 *Phys. Rev.* B **53** 8316
[40] Biljaković K, Lasjaunias J C, Zougmoré F, Monceau P, Levy F, Bernard L and Currat R 1986 *Phys. Rev. Lett.* **57** 1907
[41] Smontara A, Lasjaunias J C, Monceau P and Levy 1992 *Phys. Rev.* B **46** 12 072
Smontara A, Lasjaunias J C and Apostol M 1994 *J. Low Temp. Phys.* **7** 289

[42] Sekine T, Seino T, Izumi M and Matsuura E 1985 *Solid State Commun.* **53** 379
[43] Degiorgi L and Grüner G 1991 *Phys. Rev.* B **44** 7820
[44] Sheroni M S, Zettl A and Richards P L 1987 *Phys. Rev.* B **36** 708
[45] Degiorgi L, Alavi B, Mihaly G and Grüner G 1991 *Phys. Rev.* B **44** 7808
[46] Creager W N, Richards P L and Zettl A 1991 *Phys. Rev.* B **44** 3505
[47] Kim T W, Donovan S, Grüner G and Phipps A 1991 *Phys. Rev.* B **43** 6315
[48] Lebedev N I, Levanyuk A P and Sigov A S 1987 *Sov. Phys.–JETP* **65** 140
[49] Moussa F, Launois P, Lemée M H and Cailleau H 1987 *Phys. Rev.* B **36** 8951
[50] Cox D E, Shapiro S M, Cowley R A, Eibschutz M and Guggenheim H J 1979 *Phys. Rev.* B **19** 5754
[51] Walker M B and Gooding R J 1985 *Phys. Rev.* B **32** 7412
[52] Vallade M, Dvorak V and Lajzerowicz J 1987 *J. Physique* **48** 1171
[53] Alexandrov A S and Mott N F 1993 *Supercond. Sci. Technol.* **6** 251
Ranninger J 1994 *Physica* C **235–240** 277
[54] Aslanyan T A and Levanyuk A P 1979 *Solid State Commun.* **31** 547
Aslanyan T A, Levanyuk A P, Vallade M and Lajzerowicz J 1983 *J. Phys. C: Solid State Phys.* **16** 6705
[55] Levanyuk A P and Sannikov D G 1976 *Sov. Phys.–Solid State* **18** 1122